

Modeling dimethylsulphide production in the upper ocean

Roger A. Cropp

Faculty of Environmental Sciences, Griffith University, Nathan, Queensland, Australia

John Norbury

Mathematical Institute, University of Oxford, UK

Albert J. Gabric and Roger D. Braddock

Faculty of Environmental Sciences, Griffith University, Nathan, Queensland, Australia

Received 22 July 2003; revised 25 March 2004; accepted 25 May 2004; published 27 July 2004.

[1] Dimethylsulphide (DMS) is produced by upper ocean ecosystems and emitted to the atmosphere, where it may have an important role in climate regulation. Several attempts to quantify the role of DMS in climate change have been undertaken in modeling studies. We examine a model of biogenic DMS production and describe its endogenous dynamics and sensitivities. We extend the model to develop a one-dimensional version that more accurately resolves the important processes of the mixed layer in determining the ecosystem dynamics. Comparisons of the results of the one-dimensional model with an empirical relationship that describes the global distribution of DMS, and also with vertical profiles of DMS in the upper ocean measured at the Bermuda Atlantic Time Series, suggest that the model represents the interaction between the biological and physical processes well on local and global scales. Our analysis of the model confirms its veracity and provides insights into the important processes determining DMS concentration in the oceans.

INDEX TERMS: 0315 Atmospheric Composition and Structure: Biosphere/atmosphere interactions; 1699 Global Change: General or miscellaneous; 4805 Oceanography: Biological and Chemical: Biogeochemical cycles (1615); 4815 Oceanography: Biological and Chemical: Ecosystems, structure and dynamics; **KEYWORDS:** biogeochemical modeling, dimethylsulphide (DMS), one-dimensional model

Citation: Cropp, R. A., J. Norbury, A. J. Gabric, and R. D. Braddock (2004), Modeling dimethylsulphide production in the upper ocean, *Global Biogeochem. Cycles*, 18, GB3005, doi:10.1029/2003GB002126.

1. Introduction

[2] Dimethylsulphide (DMS) is produced by marine ecosystems from its precursor dimethylsulphoniopropionate (DMSP), abundant in phytoplankton, in sufficient concentration to sustain a net flux to the atmosphere. Once emitted to the atmosphere, DMS is oxidized to form non-sea-salt sulphate and methanesulphonate aerosols. Shaw [1983] and later Charlson *et al.* [1987] postulated that DMS-producing phytoplankton could stabilize global climate. This has led to a focus on the role of upper ocean ecosystems in shaping climate [Gabric *et al.*, 2001a].

[3] The vertical physical dynamics of the mixed layer are a critical driving force determining ecosystem dynamics in the upper ocean [Eigenheer *et al.*, 1996]; by comparison, horizontal advection is believed to have little influence on mixed layer ecosystems [Denman and Pena, 1999]. The mean irradiance field, controlled by the interaction of light penetration and the mixed layer depth, and the supply of nutrient into the mixed layer are important

limiting factors on biological production [Doney *et al.*, 1996]. Phytoplankton blooms in the ocean occur after a deepening of the mixed layer brings new nutrient to surface waters, and subsequent stratification of the surface waters traps phytoplankton in a relatively highly illuminated, high-nutrient regime, providing ideal conditions for the initiation of a phytoplankton bloom [Mann and Lazier, 1996].

[4] Shallowing of surface mixed layers also contributes to enhancing DMS production by initiating phytoplankton succession toward stronger DMSP producers, allowing a higher efficiency of conversion from DMSP to DMS, and by possibly inhibiting bacterial consumption of DMS [Simo and Pedros-Alio, 1999]. Simo and Dachs [2002] derived an empirical relationship linking chlorophyll, mixed layer depth, and DMS. Simo and Dachs contended that the relationship performed remarkably well when used to predict independent data, showing a near one-to-one correspondence between measured and predicted data, even in different biogeochemical provinces.

[5] Here we examine the dynamical properties of the Gabric *et al.* [1993] model, hereinafter referred to as the GMSK model. We initially examine the dynamics of

the depth-averaged model using the most realistic parameter set available [Gabric *et al.*, 1999]. It is essential that the endogenous dynamics of the model be understood before attempting to interpret simulation results produced by the model. This analysis elucidates the inherent attributes of the model, and reveals a relationship that may be a key to determining the model's veracity.

[6] Sensitivity analysis (SA) is one of the most important aspects of modeling systems [Oreskes *et al.*, 1994]. It may be applied to verify hypotheses inherent in the model, to calibrate models in situations where parameter values are poorly known and uncertainty exists in available data, and to identify and refine important processes [Campolongo and Saltelli, 1997]. SA is often combined with data assimilation techniques prior to models being used to simulate systems [Druon and Le Fevre, 1999; Fennel *et al.*, 2001]. SA was used in this analysis to investigate the sensitivity of the depth-averaged GMSK model to changes in parameter values and to identify the most important parameters and processes in the model.

[7] The depth-averaged GMSK model can, to some extent, include the influence of variations in mixed layer depth, as it averages over the mixed layer, but it cannot resolve or explain structures such as subsurface chlorophyll maxima commonly observed in oceans [Mann and Lazier, 1996]. One-dimensional ecosystem models resolve these effects much more accurately, and reveal the influence of exogenous physical forcings on the dynamics of the models more clearly. Edwards *et al.* [2000] noted that mixing in a simple one-dimensional ocean ecosystem model generally stabilized the model dynamics, and that the model dynamics were influenced both qualitatively and quantitatively by diffusive processes. Lefevre *et al.* [2002] reproduced the vertical structure of DMSP and DMS concentrations observed at the Bermuda Atlantic Time Series (BATS) station. They achieved this by allowing parameters in their model to vary in time as a function of irradiance and temperature, which they noted covaried with mixed layer depth.

[8] We extend the GMSK model to resolve the vertical structure of the ocean, and note the effect of the inclusion of the physical dimension on the model dynamics. We then subject the model to zonal average physical forcings and compare the one-dimensional model predictions with the empirical relationship of Simo and Dachs [2002] that synthesizes the Kettle *et al.* [1999] global DMS database. We adopted this approach in preference to comparing directly with the Kettle *et al.* database, as the latter approach would require us to calibrate the one-dimensional model over the whole globe. In addition to being a daunting computational task, there are insufficient ecosystem data available to calibrate the one-dimensional model at most localities.

[9] The one-dimensional model is forced by seasonal changes in mixed layer depth, sea surface temperature, photosynthetically available radiation, and sea surface wind speed. These forcings are calculated in latitudinal bands of 10°, and range from very large amplitude forcings in high latitudes to quite low amplitude forcings near the equator. The zonal averages allow relatively detailed comparison with the empirical relationship of Simo and Dachs [2002],

and we note that the predictions of the model correspond well with those of the empirical relationship.

[10] We also compare the one-dimensional model with vertical profiles of DMS measured as part of the BATS [Dacey *et al.*, 1998]. In contrast to the approach taken by Lefevre *et al.* [2002], we do not vary the parameters temporally to obtain the best fit but calibrate a reduced parameter set to reproduce the BATS data. We used zonal forcings for 30°N–40°N to force the model. We calibrated eight of the parameters so that the slope of the regression line, linking model-predicted DMS with the DMS concentrations measured at BATS, was approximately unity. These comparisons revealed that within its capabilities, the model reproduced the observational data well, both qualitatively and quantitatively.

[11] The application of such a suite of model analysis and comparison techniques provides useful insights into the major processes controlling DMS production in the ocean. That is, if we have a model that produces numbers that agree with the experimental data, then one major real advantage of the model is that we can examine it to see exactly why those data are produced.

2. Methods

2.1. GMSK Model

[12] The unforced equations of state of the depth-averaged GMSK model are given by equations (1)–(8) [Gabric *et al.*, 1993]. In these equations, P represents the biomass of phytoplankton, B is the biomass of bacteria, F is the biomass of flagellates, L is the biomass of large protozoa, Z is the biomass of zooplankton, N is the available nutrient, $DMSP$ is the concentration of DMSP, and DMS is the concentration of DMS. These quantities are expressed as concentrations of atomic nitrogen (mg N m^{-2}) in the cases of P , B , F , L , Z , and N , and as concentrations of atomic sulphur (mg S m^{-2}) in the cases of $DMSP$ and DMS . The model averages over the mixed layer and all concentrations and parameter values are scaled by the depth of the mixed layer.

$$\frac{dP}{dt} = k_{23} \left(\frac{N}{N + k_{24}} \right) P - k_1 \left(\frac{P}{P + k_2} \right) B - k_3 PL - k_4 PZ, \quad (1)$$

$$\begin{aligned} \frac{dB}{dt} = & k_1(1 - k_{11}) \left(\frac{P}{P + k_2} \right) B + k_{25}(1 - k_{11}) \\ & \cdot \left(\frac{N}{N + k_{26}} \right) B - k_8 \left(\frac{B}{B + k_9} \right) F - k_{10} B, \end{aligned} \quad (2)$$

$$\frac{dF}{dt} = k_8(1 - k_{14}) \left(\frac{B}{B + k_9} \right) F - k_{13} F - k_{12} FL, \quad (3)$$

$$\frac{dL}{dt} = k_{12}(1 - k_{17}) FL + k_3(1 - k_{17}) PL - k_{15} LZ - k_{16} L, \quad (4)$$

$$\frac{dZ}{dt} = k_{15}(1 - k_{20}) LZ + k_4(1 - k_{20}) PZ - k_{19} Z, \quad (5)$$

Table 1. Parameter Values Used for the GMSK Model Simulations

Parameter	Process	Units	Value
k_1	maximum rate of N uptake by B	d^{-1}	0.310
k_2	half-saturation constant for B uptake of N	mgN m^{-3}	34.650
k_3	L grazing rate (per individual) on P	$\text{m}^3 \text{mgN}^{-1} \text{d}^{-1}$	0.010
k_4	Z grazing rate (per individual) on P	$\text{m}^3 \text{mgN}^{-1} \text{d}^{-1}$	0.010
k_5	release rate of DMSP by P	d^{-1}	0.010
k_6	release rate of DMS by P	d^{-1}	0.009
k_8	maximum rate of B uptake by F	d^{-1}	1.670
k_9	half-saturation constant for F uptake of B	mgN m^{-3}	9.100
k_{10}	B specific excretion rate	d^{-1}	0.070
k_{11}	proportion of N uptake excreted by B		0.630
k_{12}	L grazing rate (per individual) on F	$\text{m}^3 \text{mgN}^{-1} \text{d}^{-1}$	0.010
k_{13}	F specific excretion rate	d^{-1}	0.050
k_{14}	proportion of N uptake excreted by F		0.650
k_{15}	Z grazing rate (per individual) on L	$\text{m}^3 \text{mgN}^{-1} \text{d}^{-1}$	0.010
k_{16}	L specific excretion rate	d^{-1}	0.050
k_{17}	proportion of N uptake excreted by L		0.650
k_{18}	DMSP excretion rate by L	d^{-1}	0.010
k_{19}	Z specific N excretion rate	d^{-1}	0.050
k_{20}	proportion of N uptake excreted by Z		0.400
k_{21}	DMSP excretion rate by Z	d^{-1}	0.010
k_{23}	maximum rate of N uptake by P	d^{-1}	0.270
k_{24}	half-saturation constant for P uptake of N	mgN m^{-3}	12.600
k_{25}	maximum rate of N uptake by B	d^{-1}	0.310
k_{26}	half-saturation constant for B uptake of N	mgN m^{-3}	3.450
k_{27}	DMSP – DMS conversion rate	d^{-1}	0.500
k_{28}	DMS consumption rate by B	d^{-1}	0.290
k_{29}	maximum DMS photo-oxidation rate	d^{-1}	1.300
k_{30}	DMS ventilation rate to atmosphere	d^{-1}	0.130
k_{31}	DMSP consumption rate by B	d^{-1}	0.530
k_{33}	phytoplankton $S(\text{DMSP}):N$ ratio		0.300
k_v	phytoplankton sinking velocity	m d^{-1}	0.500
I_s	phytoplankton saturating irradiance	W m^{-2}	60
k_w	seawater light attenuation coefficient	m^{-1}	0.045
k_p	P self-shading light coefficient	$\text{m}^2 \text{mgN}^{-1}$	0.0003
N_0	total nutrient as nitrogen	mgN m^{-3}	50–150

$$\begin{aligned}
\frac{dN}{dt} = & k_{10}B + k_{11} \left[k_{25} \left(\frac{N}{N + k_{26}} \right) B + k_1 \left(\frac{P}{P + k_2} \right) B \right] \\
& + k_{13}F + k_8k_{14} \left(\frac{B}{B + k_9} \right) F + k_{16}L \\
& + k_{17}(k_{12}FL + k_3PL) + k_{19}Z \\
& + k_{20}(k_4PZ + k_{15}LZ) - k_{23} \\
& \cdot \left(\frac{N}{N + k_{24}} \right) P - k_{25} \left(\frac{N}{N + k_{26}} \right) B,
\end{aligned} \quad (6)$$

$$\frac{d\text{DMSP}}{dt} = k_5k_{33}P + k_{18}k_{33}L + k_{21}k_{33}Z - k_{27}\text{DMSP} - k_{31}\text{DMSP}, \quad (7)$$

$$\frac{d\text{DMS}}{dt} = k_6k_{33}P + k_{27}\text{DMSP} - k_{28}\text{DMS} - k_{29}\text{DMS} - k_{30}\text{DMS}. \quad (8)$$

[13] The GMSK model details many of the fundamental processes of marine planktonic ecosystems explicitly, and consequently requires knowledge of a substantial number of biological rate constants. Several sets of parameter

values have been used in simulations with the GMSK model. For this study we have chosen the parameter value sets reported by *Gabric et al.* [1999], as they were mostly measured at the same place and time [*Matrai and Vernet*, 1997]. The parameter values measured at station one of *Gabric et al.* [1999] (Table 1) will be adopted as the best available parameter set. These values are presented in their volumetric form for consistency between the depth-averaged and one-dimensional model simulations. The depth-averaged model simulations therefore reflect sea surface conditions with an idealized mixed layer depth of 1 m.

[14] The GMSK model equations were scaled by a characteristic time (the maximum growth rate of the phytoplankton, k_{23}) and characteristic concentrations (the total nitrogen mass, N_0 , for equations (1) to (6); and the total sulphur mass, S_0 , for equations (7) and (8)). The state variables in equations (1)–(8) are replaced by their scaled versions $C' = \frac{C}{N_0}$ for $C = P, B, F, L, Z$ and N , and $C' = \frac{C}{S_0}$ where $S_0 = k_{33}N_0$ for $C = \text{DMSP}$ and DMS , and time $t' = k_{23}t$. It should be noted that the relationship between S_0 and N_0 derives from the scaling, and does not imply a Redfield ratio-type relationship. All analyses use the scaled equations.

[15] The GMSK model is essentially a nitrogen-based ecosystem model with unidirectional coupling to a sulphur-

based biochemical model. The nitrogen and sulphur models are decoupled when analyzing the dynamics.

2.2. Sensitivity Analysis

[16] The New Morris Method [Campolongo and Braddock, 1999; Cropp and Braddock, 2002] was used for the sensitivity analysis. This method uses graph theory, and in particular a solution to the “handcuffed prisoner problem” to select sampling trajectories that efficiently span the parameter space while providing for calculation of the required effects. The method also allows the calculation of the effects of individual parameters and interactions between pairs of parameters. A parameter space for the sensitivity analysis of the depth-averaged GMSK model is defined to be $\pm 25\%$ of the values used in the examination of the endogenous dynamics.

[17] The sensitivity of the model is assessed by examining changes in the annual integrated DMS flux to the atmosphere, a metric relevant to climate change considerations [Charlson et al., 1987], and utilized in previous sensitivity analyses of the model [Campolongo and Saltelli, 1997]. The DMS flux is calculated after starting a simulation with initial conditions very close to the critical point CP 1 (described in results) and integrating the full model for 1 year. This approach allowed the system to perform multiple traverses of the attractor and limited the influence of the initial conditions and transient dynamics on the annual DMS flux. As the parameter values influence the rate at which the state of the system traversed different parts of the attractor, integration over a fixed period of 1 year was considered preferable to integration over a prescribed number of circuits of the attractor.

[18] The New Morris Method generated 11,220 parameter sets, then evaluated the model and calculated the integrated annual flux of DMS to the atmosphere for each of the parameter sets. These data were used to estimate the sensitivity of the model to each of the 33 parameters, and to all 528 combinations of parameter pairs. Measures of first-order effects (μ , the mean effect of each parameter alone) and the mean second- and higher-order effects (λ , a measure of the effect of each parameter alone and in combination with all other parameters) were calculated.

2.3. One-Dimensional Model

[19] The one-dimensional GMSK model is obtained from the depth-averaged GMSK model by resolving the distribution of concentrations and fluxes over depth in the water column and allowing diffusive and advective fluxes. The model equations are now reaction-diffusion equations of the type

$$\frac{\partial C}{\partial t} = G - k_v \frac{\partial C}{\partial z} + \frac{\partial}{\partial z} D \frac{\partial C}{\partial z}, \quad (9)$$

where C is concentration, G is net production (growth – loss), k_v is the vertical advection velocity (m/day) and D is vertical turbulent diffusivity (m^2/day) [Gabric et al., 2001a]. The one-dimensional equations for each state variable have the production terms (G) in equation (9) replaced by the right-hand sides of equations (1)–(8), except that the

emission term $k_{30}\text{DMS}$ is deleted from equation (8). The emission of DMS from the sea to the air will therefore be included in the one-dimensional model as a boundary condition at the sea-air interface rather than as a sink term in the production equations. The diffusivity is a function of depth and includes uniform mixing in the mixed layer, the gradient in mixing strength that occurs at the pycnocline, and a uniform mixing profile in the sub-mixed layer. Sinking of phytoplankton is included in the model, as this is reasonably well documented [Smayda, 1970; Walsh et al., 2001], but vertical migration by zooplankton is not included, as the effect of turbulence on zooplankton feeding is not clear [Mann and Lazier, 1996]. Similarly, the effect of sedimentation of DMS when adsorbed onto particles is insignificant compared to the flux to the atmosphere and has been ignored [Jodwalis et al., 2000].

[20] The specific growth rate of phytoplankton in the one-dimensional GMSK model is subject to variation with depth due to changes in light intensity. The relationship described by Walsh et al. [2001], which includes the effects of self-shading, is used in this model:

$$R_L = \frac{I(z)}{I_s} e^{(1 - \frac{I(z)}{I_s})}, \quad (10)$$

where

$$I(z) = I_0 e^{-(k_w + k_p P)z}, \quad (11)$$

and k_w is the light attenuation of seawater, k_p is the light attenuation due to self-shading of phytoplankton, z is depth in meters, I_0 is the incident surface irradiation (W/m^2), and I_s is the phytoplankton saturating irradiation (W/m^2).

[21] Laboratory studies of phytoplankton have also revealed a dependence of phytoplankton growth rates on temperature [Eppley, 1972; Goldman and Carter, 1974]. The temperature dependence of phytoplankton growth used in this model was estimated by Eppley [1972] to be

$$R_T = e^{0.063(T - T_{\max})}, \quad (12)$$

where T is the ambient temperature ($^{\circ}\text{C}$) and T_{\max} is the maximum annual temperature. The temperature T may vary with depth, generally being uniform throughout the mixed layer with a thermocline located at about the same depth as the pycnocline separating cooler, sub-mixed layer water [Mann and Lazier, 1996].

[22] The upper boundary of the model is formed by the sea surface (i.e., the sea-air interface), and the lower boundary is set at 200 m, about 25% deeper than the maximum of the deepest mixed layer or euphotic depth measured at the geographic locations to be simulated. The region of the water column below the mixed layer acts as a reservoir of nutrient that may be entrained into the mixed layer when it deepens. This scenario allows the model to reproduce the physical mechanisms that initiate phytoplankton blooms [Mann and Lazier, 1996].

[23] The boundary condition for equation (9) is given by [Gabric and Parslow, 1989]

$$(1 - \xi)k_v C - D \frac{\partial C}{\partial z} = 0, \quad (13)$$

where ξ is a parameter specifying the nature of the boundary. If $k_v \neq 0$, a perfectly absorbing boundary is specified when $\xi = 1$, and a perfectly reflecting boundary is specified when $\xi = 0$. A mass-conservative ecosystem model is desirable so that the model biotic compartments do not eventually run out of nutrient. A mass conservative ecosystem model also accords with the findings of *Spitz et al.* [2001] that some ecosystem models fit real data best if mass is approximately conserved. Zero-flux boundary conditions are therefore implemented for the state variables on both boundaries with the exception of P at the bottom boundary and DMS at the top boundary.

[24] Phytoplankton sink through the water column and out of the upper, photic zone, and contribute to “marine snow” that delivers nutrient to the deep ocean [*Smayda*, 1970]. The nutrient lost as phytoplankton is eventually replaced by processes such as upwellings associated with the divergence of the Ekman transport [*Pond and Pickard*, 2000] that deliver inorganic nutrients back to the upper ocean. The Joint Global Ocean Flux Study (JGOFS), in a comparison of one-dimensional biogeochemical models of the upper ocean [*Evans and Garcon*, 1997], concluded that the bottom boundary condition should allow the sinking flux of phytoplankton to pass through it. The mass falling through the bottom boundary should be reinjected into the sub-mixed layer as nutrient to simulate Ekman upwelling. The bottom boundary condition for P is therefore given by the perfectly absorbing version of equation (13).

[25] The primary intent of the model is to estimate DMS transfer from the ocean to the atmosphere across the sea-air interface. The *Liss and Merlivat* [1986] model of gas transfer rate will be used as a boundary condition for the one-dimensional model. The Liss and Merlivat parameterization is appropriate for the principal application of this model (investigating the potential for biogenic DMS to mitigate climate change), as it provides the most conservative flux estimates of the parameterizations currently available [*Kettle and Andreae*, 2000]. As it conservatively estimates the sea-air flux, the parameterization will consequently slightly exaggerate sea surface DMS concentrations. However, as will be seen later, this effect is insignificant compared to variations due to uncertainties in values of some process parameters.

[26] The atmospheric concentration of DMS is approximately zero compared to the aqueous concentration [*Liss and Merlivat*, 1986], so the sea-air flux of DMS may be parameterized as

$$F_{\text{vent}} = k_{\text{tr}} \text{DMS}. \quad (14)$$

The boundary condition for DMS at the top boundary is therefore the condition

$$\frac{d\text{DMS}}{dz} = k_{\text{tr}} \text{DMS}. \quad (15)$$

The piston velocity (k_{tr}) is calculated from three equations representing different sea state/wind speed (w) scenarios. These are: a smooth surface regime ($w = 0-3.6 \text{ m s}^{-1}$), a

rough surface regime ($w = 3.6-13 \text{ m s}^{-1}$), and a breaking wave regime ($w > 13 \text{ m s}^{-1}$):

$$\begin{aligned} k_{\text{tr}} &= 0.17aw & w \leq 3.6 \text{ m s}^{-1}, \\ k_{\text{tr}} &= b(2.85w - 10.3) + 0.6a & 3.6 < w \leq 13 \text{ m s}^{-1}, \\ k_{\text{tr}} &= b(5.9w - 49.9) + 0.6a & w > 13 \text{ m s}^{-1}, \end{aligned} \quad (16)$$

where

$$\alpha = \left(\frac{600}{Sc}\right)^{2/3} \text{ and } \beta = \sqrt{\frac{600}{Sc}}.$$

[27] The dimensionless Schmidt number (Sc) is the ratio of the absolute viscosity of seawater to the diffusivity of DMS in water. For a given gas, the Schmidt number decreases with increasing water temperature. The dependence of Sc on sea surface temperature for DMS has been experimentally derived by *Saltzman et al.* [1993],

$$Sc = 2674.0 - 147.12 \times \text{SST} + 3.726 \times \text{SST}^2 - 0.038 \times \text{SST}^3. \quad (17)$$

[28] The Method of Lines [*Schuesser*, 1991, 1994] was used to solve the partial differential equations of the one-dimensional model. This method represents derivatives in the spatial dimension by finite difference approximations, and then treats the problem as a system of coupled time-dependent ordinary differential equations at each grid point. An adaptive step size integrator such as a Runge-Kutta can then be used to efficiently advance the solution in time at each point in the water column. The accuracy and stability characteristics of the method are easily controlled [*Schuesser*, 1991] and the spatial discretization is a conceptually convenient organization for the solution of models with one physical dimension.

[29] A sigmoid function (equation (18)) is used to generate a diffusivity profile for use in the model simulations,

$$D = \frac{D_{\text{max}} + D_{\text{min}} e^{r(D_{\text{min}} - D_{\text{max}})(\frac{2(z - \text{MLD})}{H})}}{1 + e^{r(D_{\text{min}} - D_{\text{max}})(\frac{2(z - \text{MLD})}{H})}}, \quad (18)$$

where D is the diffusivity (m^2/day), D_{max} is the maximum mixed layer diffusivity ($0 < D_{\text{max}} < \sim 1000$), D_{min} is the minimum sub-mixed layer diffusivity ($0 < D_{\text{min}} < \sim 10$), and z is the depth in the water column (meters). The depth of the model domain is H (meters), and MLD is the depth of the mixed layer (meters). The quantity r (day/m^2) is a parameter that controls the steepness of the pycnocline ($1 < r < 50$), where $r \sim 20$ generates pycnoclines typical of those observed in the ocean. The use of this sigmoid function assumes homogeneity of all properties within the mixed layer, which is considered realistic except perhaps for conditions of deep convective mixing [*Martin*, 1985, 1986].

[30] An analogous function is used to describe the vertical temperature profile. The temperature of the mixed layer (T_{max}) is also assumed to be homogeneous, and the sub-

mixed layer temperature (T_{\min}) is held constant. A temperature profile is calculated using equation (19),

$$T = \frac{T_{\max} + T_{\min} e^{r(T_{\min} - T_{\max}) \left(\frac{2(z - \text{MLD})}{H} \right)}}{1 + e^{r(T_{\min} - T_{\max}) \left(\frac{2(z - \text{MLD})}{H} \right)}}. \quad (19)$$

The temperature limitation factor R_T that operates on P growth is then calculated by using the temperature (T) calculated from equation (19) in equation (12).

[31] The one-dimensional model equations are scaled by characteristic concentrations: The total nitrogen mass (N_0) is used to scale the sulphur-based equations, and a characteristic sulphur mass (S_0) is used to scale the sulphur-based equations. A characteristic sulphur mass is selected so that $S_0 = k_{33}N_0$, and k_{33} (the phytoplankton sulphur as DMSP to nitrogen ratio) may be canceled from the scaled sulphur equations. Depth is scaled by the simulation depth of the model, H (i.e., $z' = \frac{z}{H}$), the maximum annual mixed layer diffusivity D_{\max} (i.e., $D' = \frac{D}{D_{\max}}$) and a characteristic time T (i.e., $t' = \frac{t}{T}$). A characteristic time is selected so that $T = \frac{H^2}{D_{\max}}$.

[32] *Simo and Dachs* [2002] examined 2385 sea surface DMS measurements that had accompanying chlorophyll concentration measurements from the over 15,000 DMS measurements compiled in the *Kettle et al.* [1999] database. They added to these climatological mixed layer depth measurements developed by Samuels and Cox and derived an empirical relationship linking chlorophyll, mixed layer depth and DMS. *Simo and Dachs* [2002] derived two relationships that could predict sea surface DMS concentrations from the mixed layer depth and surface chlorophyll concentration,

$$\text{DMS} = -\ln(\text{MLD}) + 5.7 \quad \frac{\text{CHL}}{\text{MLD}} < 0.02 \quad (20)$$

$$\text{DMS} = 55.8 \left(\frac{\text{CHL}}{\text{MLD}} \right) + 0.6 \quad \frac{\text{CHL}}{\text{MLD}} \geq 0.02, \quad (21)$$

where the units of MLD are meters, CHL are mg/m^3 , and DMS are nanomoles (nM).

[33] Equations (20) and (21) provide an efficacious method of comparing the predictions of the one-dimensional model with the global DMS database. The surface DMS concentrations predicted by the one-dimensional model are compared to DMS concentrations predicted by equations (20) and (21) using the mixed layer depths used to force the models and the surface P predicted by them. The nondimensional P predicted by the model was converted to a carbon concentration and then to a chlorophyll concentration by using a Redfield ratio nitrogen to carbon conversion of 0.175 (by weight) and a carbon to chlorophyll ratio of 50 [Gabric et al., 2001b]. The resultant time series of chlorophyll concentration was used with the time series of mixed layer depth in equations (20) and (21) to predict DMS.

[34] The DMS sea surface concentrations predicted by the model are compared with those predicted by equations (20) and (21) for fourteen 10° zones of latitude between 70°N and 70°S . This latitude range was chosen as mixed layer climatologies are unreliable outside this range [Goyet et al., 2000].

[35] The one-dimensional model was run in two simulation scenarios. Initially the model was run in a 100-m-deep environment with a static light field that attenuated exponentially with depth. A static mixed layer at 50 m separated a high-diffusion ($1000 \text{ m}^2/\text{day}$) mixed layer from a low-diffusion ($1 \text{ m}^2/\text{day}$) sub-mixed layer. Temperature was constant over depth and time, and the parameter set specified in Table 1 was used. This simulation was used to compare the one-dimensional model dynamics with those observed for the depth-averaged model.

[36] A second simulation scenario in which the model was subject to a set of zonally averaged seasonal forcings was considered. The model was forced in each zone with seasonal variations in sea surface temperature (Figure 1), mixed layer depth (Figure 2), photosynthetically available radiation (Figure 3), and sea surface wind (Figure 4). Mixed layer diffusivity was constant at $250 \text{ m}^2/\text{day}$, which was sufficient to homogenize the mixed layer chlorophyll concentration. The sub-mixed layer diffusivity was constant at $1 \text{ m}^2/\text{day}$. The sea surface temperature climatology was derived from 15 years of AVHRR data, the mixed layer depth was derived from the Carbon Dioxide Information Analysis Center reanalysis of WOA94 data [Goyet et al., 2000], the photosynthetically available radiation from 4 years of SeaWiFS data and the wind speed from 2 years of SeaWinds data. A water column depth of 200 m and the parameter set specified in Table 1 was used. The simulations were run for 730 days, commencing in winter (1 January in the Northern Hemisphere and 1 July in the Southern Hemisphere), and used the same initial conditions. The second 365 days of these simulations were used to compare the DMS predicted by the model to that predicted by *Simo and Dachs* [2002].

[37] We also compare the one-dimensional model with vertical profiles of DMS measured as part of the BATS [Dacey et al., 1998]. The BATS data used in this analysis comprised 247 measurements of DMS taken in the top 100 m of the water column on 27 days spaced at irregular intervals (1–33 days apart) over a 12-month period. DMS measurements were usually made at depths of 1, 5, 10, 15, 20, 30, 40, 60, 80, and 100 m.

[38] The one-dimensional GMSK model was forced with zonal forcings for 30°N – 40°N (Figures 1–4), and equation (18) was used to represent the diffusivity profile. The model was integrated for 730 days, with the second 365 days (366–730) being used to compare with the BATS data. We used a genetic algorithm [Holland, 1975] to calibrate eight of the 33 model parameters to minimize the squared error between the model and BATS data at the 247 BATS data points. We also calibrated the phytoplankton sulphur (as DMSP) to nitrogen ratio so that the slope of the regression line linking the DMS concentration predicted by the model and the BATS DMS concentration was approximately unity.

3. Results

3.1. Nitrogen Submodel

3.1.1. Dynamics

[39] Numerical integration of the nitrogen submodel reveals that its dynamics lie on an attractor that can be described in PZB and BFN spaces (Figures 5a and 5b). The

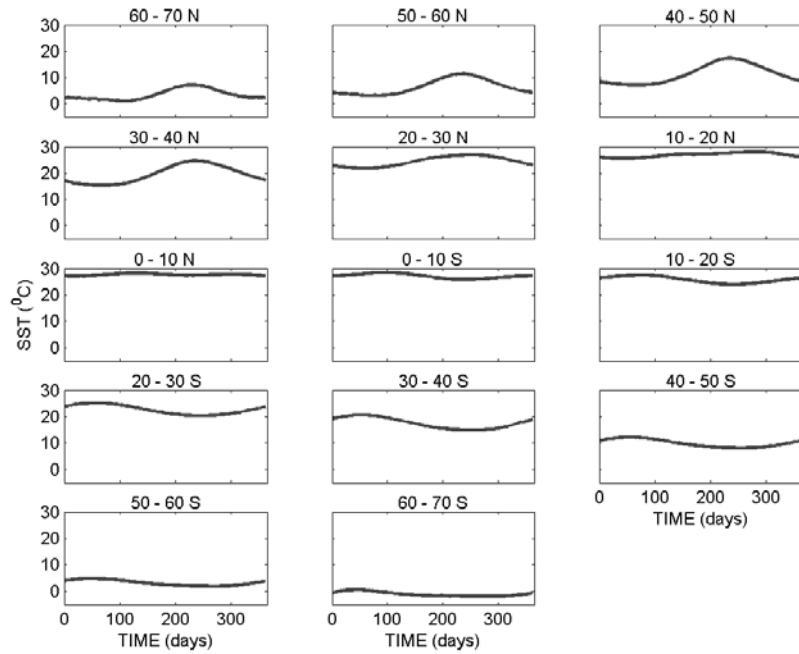


Figure 1. Zonal forcings of sea surface temperature (SST) used in simulations. See color version of this figure in the HTML.

system traverses *PZB* space by spiraling in toward the point labeled CP 1 in Figure 5a, then moving away from it as bacteria bloom to a point in which bacteria contain approximately 90% of the total nutrient (CP 2). This is followed by a precipitous bacterial population crash as bacteria are

grazed by flagellates. This is evident in Figure 5a as the part of the trajectory from the maximum bacterial concentration (CP 2) toward the origin, and in Figure 5b as the diagonal line falling from left to right toward CP 3. The latter figure also reveals the increased population of flag-

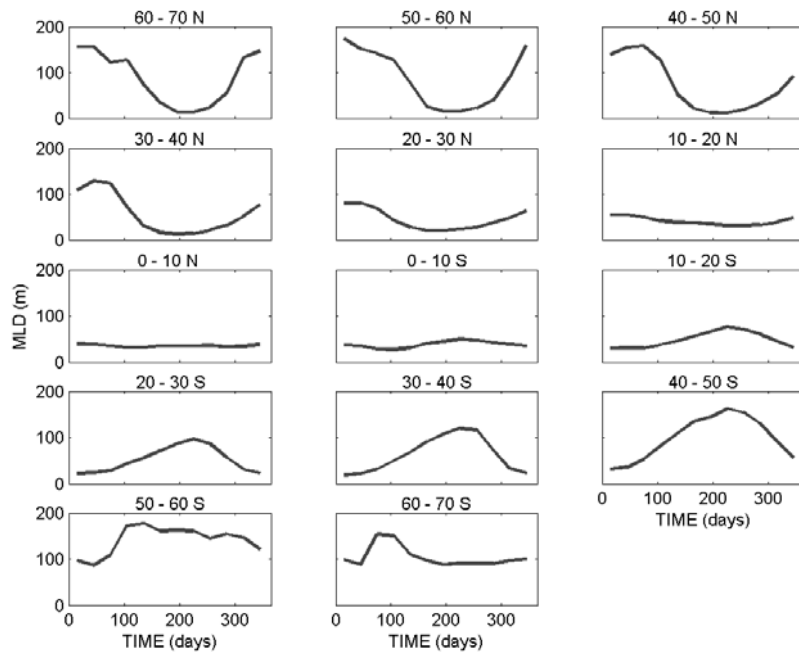


Figure 2. Zonal forcings of mixed layer depth (MLD) used in simulations. See color version of this figure in the HTML.

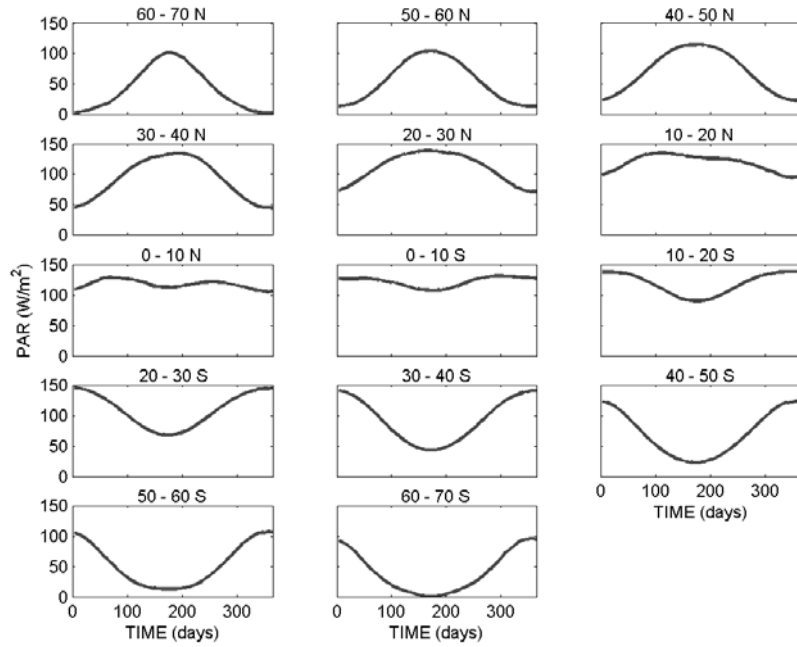


Figure 3. Zonal forcings of photosynthetically available radiation (PAR) used in simulations. See color version of this figure in the HTML.

ellates not evident in Figure 5a. The flagellate population is subsequently converted to nutrient via mortality after its only food source, bacteria, is exhausted. This is the lower rear point of the state-space cubes in Figures 5a and 5b (CP 4). The subsequent uptake of nutrient by phytoplankton initiates new oscillations represented in Figures 5a and 5b

by travel along the trajectories from the rear, center corner to the lower left corner of the state-spaces (CP 5). The system then approaches CP 1 again.

[40] The integration reveals that L falls rapidly to very low levels, and does not influence the dynamics of the model at all. An approximate analysis suggests that there are

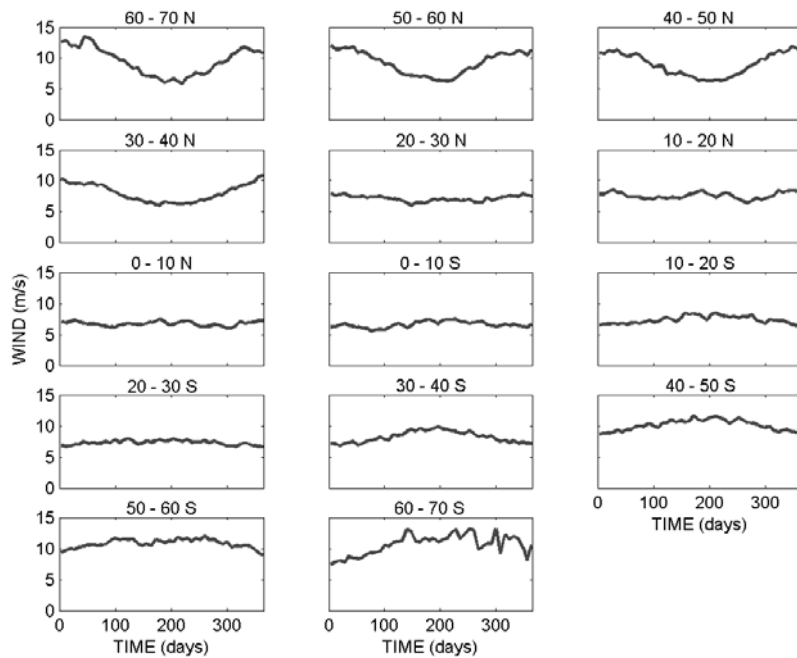


Figure 4. Zonal forcings of sea surface wind used in simulations. See color version of this figure in the HTML.

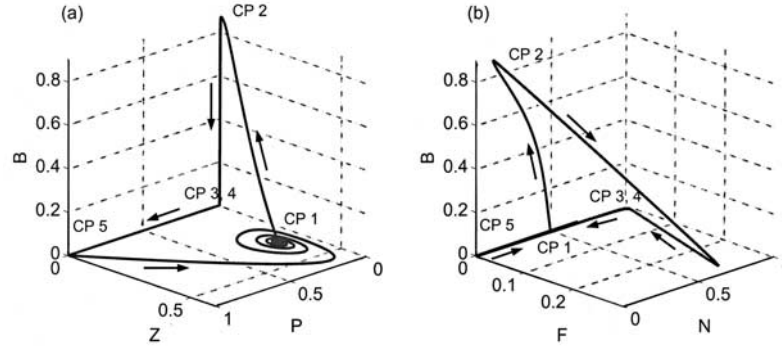


Figure 5. Attractor of the GMSK model shown in (a) *PZB* state-space and (b) *FNB* state-space.

few circumstances in which L can grow. When B and F are small, as they are most of the time, then L grows like

$$\frac{dL}{dt} \approx (0.65P - 1.85Z - 0.185)L; \quad (22)$$

that is, L will only grow if

$$P > 2.85Z + 0.285. \quad (23)$$

[41] It is apparent from Figure 5a that only a small portion of the attractor (the region around CP 5) satisfies equation (23). The system resides in this region of state-space for only a very small proportion of the time it takes to complete one circuit of the attractor. At all other times, the approximate analysis suggests that L will be decaying quickly and will always go extinct. The model may therefore really be a *PBFZN* system. This does not suggest that large protozoa (L) are not important in real marine ecosystems, but that the formulation of the GMSK model renders a separate state variable for them redundant. This may be considered to indicate that L are implicitly included in a general zooplankton guild (Z). The equation of state describing the time variation in L (equation (4)) is then deleted from the system, as are terms involving L in the other equations of state.

3.1.2. Steady States

[42] The steady states (equilibria or critical points) of the unforced nitrogen components of the GMSK model, denoted by P^* , B^* , F^* , Z^* and N^* , are obtained by setting the time derivatives to zero (i.e., $\frac{dP}{dt} = 0$, etc.) and solving the resultant system of equations. When solving this system of equations, it turns out that the P^* steady state is obtained from the Z equation of state and Z^* is obtained from the P equation of state. Likewise, B^* is obtained from the F equation of state and F^* is obtained from the B equation of state. Equations (24)–(27) with the positive root from equation (28) describe the critical point labeled CP 1 in Figures 5a and 5b.

$$P^* = \frac{k_{19}}{k_4(1 - k_{20})}, \quad (24)$$

$$B^* = \frac{k_9 k_{13}}{k_8(1 - k_{14}) - k_{13}}, \quad (25)$$

$$F^* = \left(\frac{B^* + k_9}{k_8} \right) \left[k_1(1 - k_{11}) \left(\frac{P^*}{P^* + k_2} \right) + k_{25}(1 - k_{11}) \left(\frac{N^*}{N^* + k_{26}} \right) - k_{10} \right], \quad (26)$$

$$Z^* = \left(\frac{k_{23}}{k_4} \right) \left(\frac{N^*}{N^* + k_{24}} \right) - \left(\frac{k_1}{k_4} \right) \left(\frac{B^*}{P^* + k_2} \right), \quad (27)$$

$$\begin{aligned} & N^{*3} + N^{*2}[P^* + B^* + \alpha_R + \beta_R + \delta_R + k_{24} + k_{26} - \chi_R - \varepsilon_R - N_0] \\ & + N^*[k_{24}k_{26} + (k_{24} + k_{26})(P^* + B^* + \alpha_R - \chi_R - \varepsilon_R - N_0) \\ & + k_{24}\beta_R + k_{26}\delta_R] + k_{24}k_{26}(P^* + B^* + \alpha_R - \chi_R - \varepsilon_R - N_0) \\ & = 0, \end{aligned} \quad (28)$$

where

$$\alpha_R = k_1(1 - k_{11}) \left(\frac{P^*}{P^* + k_2} \right) \left(\frac{B^* + k_9}{k_8} \right),$$

$$\beta_R = k_{25}(1 - k_{11}) \left(\frac{B^* + k_9}{k_8} \right), \quad \chi_R = k_{10} \left(\frac{B^* + k_9}{k_8} \right),$$

$$\delta_R = \frac{k_{23}}{k_4} \quad \text{and} \quad \varepsilon_R = \frac{k_1}{k_4} \left(\frac{B^*}{P^* + k_2} \right).$$

[43] The point labeled CP 2 in Figures 5a and 5b is the critical point described by equations (29) and (30),

$$\begin{aligned} P^* &= 0, \\ F^* &= 0, \\ Z^* &= 0, \end{aligned} \quad (29)$$

$$\begin{aligned} B^* &= N_0 - \frac{k_{10}k_{26}}{k_{25}(1 - k_{11}) - k_{10}}, \\ N^* &= \frac{k_{10}k_{26}}{k_{25}(1 - k_{11}) - k_{10}}. \end{aligned} \quad (30)$$

[44] Similarly, the point labeled CP 3 in Figures 5a and 5b is the critical point described by equations (31)–(33) with the positive root from equation (34).

$$\begin{aligned} P^* &= 0 \\ Z^* &= 0, \end{aligned} \quad (31)$$

$$B^* = \frac{k_9 k_{13}}{k_8(1 - k_{14}) - k_{13}}, \quad (32)$$

$$F^* = \frac{k_{25}}{k_8}(1 - k_{11})(B^* + k_9) \left(\frac{N^*}{N^* + k_{26}} \right) - \frac{k_{10}}{k_8}(B^* + k_9), \quad (33)$$

$$N^* = \frac{1}{2} \left[\begin{aligned} & - \left(k_{26} + B^* + \left(\frac{B^* + k_9}{k_8} \right) (k_{10} + k_{25}(1 - k_{11})) - N_0 \right) \\ & \pm \sqrt{\left(k_{26} + B^* + \left(\frac{B^* + k_9}{k_8} \right) (k_{10} + k_{25}(1 - k_{11})) - N_0 \right)^2 - 4k_{26} \left(B^* \left(1 + \frac{k_{10}}{k_8} \right) + \frac{k_9 k_{10}}{k_8} - N_0 \right)} \end{aligned} \right]. \quad (34)$$

[45] The point labeled CP 4 in Figure 5b is described by equation (35), where all biota are extinct.

$$\begin{aligned} P^* &= 0, \\ B^* &= 0, \\ F^* &= 0, \\ Z^* &= 0, \\ N^* &= N_0. \end{aligned} \quad (35)$$

[46] Similarly, the point labeled CP 5 in Figures 5a and 5b is the critical point given by equation (36) where phytoplankton contain all the nutrient, and all other species are extinct,

$$\begin{aligned} P^* &= N_0, \\ B^* &= 0, \\ F^* &= 0, \\ Z^* &= 0, \\ N^* &= 0. \end{aligned} \quad (36)$$

3.1.3. Stability

[47] The stability characteristics of the model in the regions around the critical points may be assessed by examining the eigenvalues of the Jacobian matrix obtained by linearizing the system. Positive eigenvalues indicate

Table 2. Stability Properties of the Nitrogen Models

CP	GMSK	PZN	BFN
1	saddle	stable spiral point	
2	saddle		unstable node
3	saddle		unstable spiral point
4	saddle	saddle	saddle
5	saddle	saddle	

unstable critical points, and negative eigenvalues indicate stable critical points [Boyce and DiPrima, 1997]. The eigenvalues and eigenvectors of the linearized model were obtained numerically by evaluating the Jacobian matrix at each of the critical points. A summary of the stability properties of the critical points are shown in Table 2.

[48] All the critical points (CP 1–5) have at least one unstable manifold that directs the system flow on to the next critical point associated with the attractor. Evaluation of equations (24)–(36) reveals that all critical points with the exception of CP 3 are located very close to the attractor. The attractor does not closely approach CP 3 due to the flow from CP 2 being directed toward CP 3 along a stable manifold of CP 3 that lies very close to an unstable manifold (of CP 3). An approximate analysis of the model dynamics in the region of CP 3 reveals that when B is approximately zero,

$$\frac{dF}{dt} \approx -0.1F, \Rightarrow F \approx F_b e^{-0.1(t-t_b)}, \quad (37)$$

and when $B > 0.1$,

$$\frac{dF}{dt} \approx F, \Rightarrow F \approx F_c e^{t-t_c}. \quad (38)$$

[49] Equation (37) indicates that while B is very small, F will be maintained at very low levels. Once B starts to grow, equation (38) then controls the growth of F , and F will begin to grow like e^t . However, in order for B to grow, it must first escape the control of F . Equation (39) reveals that when F falls to sufficiently low values, and P and N are not near-zero (i.e., $P > 0.1$ and $N > 0.1$), B can escape F 's control, and will grow like $e^{0.25t}$,

$$\frac{dB}{dt} \approx 0.25B - 2F, \Rightarrow B \approx B_c e^{0.25(t-t_c)} - 4F_c e^{t-t_c}. \quad (39)$$

[50] F must eventually overtake B , initially because its growth rate is much faster (e^t versus $e^{0.25t}$), but also because it preys on B , causing B to decline like $4e^t$. F is therefore able to drive B to very low levels very quickly, and hold B there while it slowly decays like $e^{-0.1t}$. B is preyed on only by F , and F is not subject to predation, but decays through natural mortality due to exhaustion of its food source. All the production of B and F is therefore rapidly transformed into N (i.e., the system approaches CP 4).

[51] For the majority of the simulation time, the trajectory of the system lies on the region of the attractor where the system is asymptotically approaching the critical point CP 1. It is pertinent to now recall that for critical point CP 1, P^* is obtained from the Z equation of state, Z^* is obtained from the P equation of state, B^* is obtained from the F equation

of state, and F^* is obtained from the B equation of state. This suggests that the model may effectively split into a PZN subsystem and a BFN subsystem that are coupled only through a single flux, the predation of B on P , and a shared nutrient pool, N . The dynamics observed in the GMSK model may then be a reflection of the interaction of these two subsystems. A hypothesis following from this suggestion states that the characteristics of the different parts of the attractor stem from the relative amounts of control each subsystem exerts on the overall dynamics. This will be examined by investigating the attractors of the two subsystems.

3.1.4. PZN Subsystem

[52] The PZN subsystem is given by equations (40)–(42),

$$\frac{dP}{dt} = k_{23} \left(\frac{N}{N + k_{24}} \right) P - k_4 PZ, \quad (40)$$

$$\frac{dZ}{dt} = k_4(1 - k_{20})PZ - k_{19}Z, \quad (41)$$

$$\frac{dN}{dt} = k_{19}Z + k_4 k_{20} PZ - k_{23} \left(\frac{N}{N + k_{24}} \right) P. \quad (42)$$

[53] The PZN model has four critical points, described by equations (43) and (44), and equations (47)–(49). Equation (43) is the same as CP 4 of the GMSK model, and equation (44) is the same as CP 5 of the GMSK model.

$$\begin{aligned} P^* &= 0, \\ Z^* &= 0, \end{aligned} \quad (43)$$

$$\begin{aligned} N^* &= N_0, \\ P^* &= N_0, \\ Z^* &= 0, \\ N^* &= 0. \end{aligned} \quad (44)$$

[54] The eigenvalues of the linearized system about the critical point described by equation (43) are

$$\begin{aligned} \lambda_{PZN_1} &= k_{23} \left(\frac{N^*}{N^* + k_{24}} \right) \\ \lambda_{PZN_2} &= -k_{19}. \end{aligned} \quad (45)$$

As λ_{PZN_1} is always positive for realistic values of N^* and λ_{PZN_2} is always negative, the critical point described by equation (43) is always a saddle point. Similarly, the eigenvalues of the linearized system around the critical point described by equation (44) are

$$\begin{aligned} \lambda_{PZN_3} &= -\frac{k_{23}P^*}{k_{24}} \\ \lambda_{PZN_4} &= k_4(1 - k_{20})P^* - k_{19}. \end{aligned} \quad (46)$$

Again, λ_{PZN_3} is always negative and λ_{PZN_4} is always positive for realistic values of P^* , and the critical point described by equation (44) is always a saddle point.

[55] Equations (47)–(49) (using the positive root of equation (49)) describe a point that is very similar to CP 1 of the GMSK model. The steady state P concentration is the same in both models, and the Z steady state concentration differs by a small amount proportional to B^* , i.e.,

$$P^* = \frac{k_{19}}{k_4(1 - k_{20})}, \quad (47)$$

$$Z^* = \frac{k_{23}}{k_4} \left(\frac{N^*}{N^* + k_{24}} \right), \quad (48)$$

$$\begin{aligned} N^* &= \frac{1}{2} \left[- \left(k_{24} + P^* + \frac{k_{23}}{k_4} - N_0 \right) \right. \\ &\quad \left. \pm \sqrt{\left(k_{24} + P^* + \frac{k_{23}}{k_4} - N_0 \right)^2 - 4k_{24}(P^* - N_0)} \right]. \end{aligned} \quad (49)$$

[56] The eigenvalues of the linearized PZN system about this critical point are

$$\begin{aligned} \lambda_{PZN_5,6} &= -\frac{k_{23}P^*}{2} \left[\frac{k_{24}}{(N^* + k_{24})^2} \right] \\ &\quad \cdot \left\{ 1 \pm \sqrt{1 - (N^* + k_{24}) \left[1 + \frac{(N^* + k_{24})^2}{k_{23}k_{24}P^*} \right] \left(\frac{4k_{19}N^*}{k_{24}P^*} \right)} \right\}. \end{aligned} \quad (50)$$

The stability of this critical point will depend on the value of the discriminant (χ_{PZN}) of the eigenvalues,

$$\chi_{PZN} = (N^* + k_{24}) \left[1 + \frac{(N^* + k_{24})^2}{k_{23}k_{24}P^*} \right] \left(\frac{4k_{19}N^*}{k_{24}P^*} \right). \quad (51)$$

The steady state will be a saddle point if $\chi_{PZN} < 0$ [Boyce and DiPrima, 1997]. The dynamics of the steady state for $\chi_{PZN} > 0$ are proper node if $0 < \chi_{PZN} < 1$, node if $\chi_{PZN} = 1$, and spiral point if $\chi_{PZN} > 1$. The dynamics near the critical point described by equations (47) and (48) with the positive root of equation (49) will be stable for all $\chi_{PZN} > 0$, as the real part of the eigenvalues, given by

$$\text{Re}(\lambda_{PZN_5,6}) = -\frac{k_{23}}{2} \left[\frac{k_{24}}{(N^* + k_{24})^2} \right] P^* \quad (52)$$

is always negative for positive parameters and state variables. The critical point is a stable spiral node as $\lambda_{PZN} \gg 1$ for the parameter set used throughout this analysis. The stability of the other critical point described by equations (47)–(49) is not of interest as equation (49) indicates that this involves negative concentrations and is therefore not realistic.

[57] The similarity of the analytic expressions for P^* and Z^* for the critical point CP 1 of the GMSK model and the critical point of the PZN subsystem (equations (24) and (47), and equations (27) and (48), respectively) indicates

that the *PZN* and *GMSK* models are very closely related. This close relationship is further supported by the two models sharing the critical points CP 4 and CP 5. The stability of these critical points is the same (both are saddle points) for the *GMSK* and *PZN* models (Table 2).

[58] The stability characteristics of CP 1 and its equivalent in the *PZN* subsystem are also very similar, with both being spiral nodes. The coupling to the *BFN* subsystem and the consequent presence of B^* in equation (27), while precipitating only a slight difference in the values of the state variables at the respective critical points, has profound implications for the stability characteristics of the *GMSK* model.

3.1.5. *BFN* Subsystem

[59] The *BFN* subsystem is given by the following equations:

$$\frac{dB}{dt} = k_{25}(1 - k_{11})\left(\frac{N}{N + k_{26}}\right)B - k_8\left(\frac{B}{B + k_9}\right)F - k_{10}B, \quad (53)$$

$$\frac{dF}{dt} = k_8(1 - k_{14})\left(\frac{B}{B + k_9}\right)F - k_{13}F, \quad (54)$$

$$\frac{dN}{dt} = k_{10}B + k_{13}F + k_8k_{14}\left(\frac{B}{B + k_9}\right)F - k_{25}(1 - k_{11})\left(\frac{N}{N + k_{26}}\right)B. \quad (55)$$

[60] The *BFN* subsystem also has four critical points, described by equations (56), (59)–(61) and (64)–(66). The critical point described by equation (56) is the same as CP 4 of the *GMSK* model and equation (43) of the *PZN* subsystem,

$$\begin{aligned} B^* &= 0, \\ F^* &= 0, \end{aligned} \quad (56)$$

$$N^* = N_0.$$

The eigenvalues of the linearized system about the critical point described by equation (56) are

$$\lambda_{BFN_1} = k_{25}(1 - k_{11})\left(\frac{N^*}{N^* + k_{26}}\right) - k_{10}, \quad (57)$$

$$\lambda_{BFN_2} = -k_{13}. \quad (58)$$

λ_{BFN_1} will be positive and λ_{BFN_2} negative for all realistic parameter values, and the critical point described by equation (56) will therefore always be a saddle point.

[61] The point described by equations (59)–(61) is the same as CP 2 of the *GMSK* model,

$$B^* = N_0 - N^*, \quad (59)$$

$$F^* = 0, \quad (60)$$

$$N^* = \frac{k_{10}k_{26}}{k_{25}(1 - k_{11}) - k_{10}}. \quad (61)$$

The eigenvalues of the linearized system about this critical point are

$$\lambda_{BFN_3} = k_{25}(1 - k_{11})\left(\frac{N^{*2} + k_{26}(N^* + B^*)}{(N^* + k_{26})^2}\right) - k_{10}, \quad (62)$$

$$\lambda_{BFN_4} = k_8(1 - k_{11})\left(\frac{B^*}{B^* + k_9}\right) - k_{13}. \quad (63)$$

In this case, both λ_{BFN_3} and λ_{BFN_4} will be positive for all realistic parameter values, and the critical point described by equations (59)–(61) will always be an unstable node.

[62] The critical point described by equations (64)–(66) (using the positive root of equation (66)) is the same as CP 3 of the *GMSK* model,

$$B^* = \frac{k_9k_{13}}{k_8(1 - k_{14}) - k_{13}}, \quad (64)$$

$$F^* = \frac{k_{25}}{k_8}(1 - k_{11})(B^* + k_9)\left(\frac{N^*}{N^* + k_{26}}\right) - \frac{k_{10}}{k_8}(B^* + k_9), \quad (65)$$

$$N^* = \frac{1}{2} \left[\begin{aligned} & -\left(k_{26} + B^* + \left(\frac{B^* + k_9}{k_8}\right)(k_{10} + k_{25}(1 - k_{11})) - N_0\right) \\ & \pm \sqrt{\left(k_{26} + B^* + \left(\frac{B^* + k_9}{k_8}\right)(k_{10} + k_{25}(1 - k_{11})) - N_0\right)^2 - 4k_{26}\left(B^*\left(1 + \frac{k_{10}}{k_8}\right) + \frac{k_9k_{10}}{k_8} - N_0\right)} \end{aligned} \right]. \quad (66)$$

[63] The eigenvalues of the linearized *BFN* subsystem about this critical point are

$$\begin{aligned} \lambda_{BFN_5,6} &= \left[k_8\left(\frac{B^*}{(B^* + k_9)^2}\right) - k_{25}(1 - k_{11}) \right. \\ & \quad \left. \cdot \left(\frac{k_{26}}{(N^* + k_{26})^2}\right)B^* \right] \left\{ 1 \pm \sqrt{1 - \chi_{BFN}} \right\}, \end{aligned} \quad (67)$$

where χ_{BFN} is the discriminant of the eigenvalues, and

$$\begin{aligned} \chi_{BFN} &= \frac{4 \left[k_{25}(1 - k_{11})\left(\frac{k_{26}}{(N^* + k_{26})^2}\right)B^* + k_8\left(\frac{B^*}{(B^* + k_9)^2}\right) \right] \left[k_8(1 - k_{14})\left(\frac{k_9}{(B^* + k_9)^2}\right)F^* \right]}{\left[k_8(1 - k_{14})\left(\frac{B^*}{(B^* + k_9)^2}\right)F^* - k_{25}(1 - k_{11})\left(\frac{k_{26}}{(N^* + k_{26})^2}\right)B^* \right]^2}. \end{aligned} \quad (68)$$

[64] The stability of this critical point of the *BFN* subsystem is subject to the same criteria described for the critical point described by equations (47)–(49) of the *PZN* subsystem described above. The stability properties of the critical point described by equations (64)–(66) are not

obvious from the analytic expressions for the eigenvalues. However, it is apparent from equation (68) that c_{BFN} will always be positive, and therefore the critical point can never be a saddle point. Evaluation of equations (67) and (68) using the parameter values in Table 1 indicates that $\text{Re}(\lambda_{\text{BFN}})$ is positive ($\cong 2.55$), and c_{BFN} is also large ($\cong 9$) and the point is an unstable spiral node.

[65] The critical points of the *BFN* subsystem have less stable characteristics than the analogous critical points of the *GMSK* model. CP 2 and 3 are saddle points in the *GMSK* model, but are unstable nodes in the *BFN* subsystem. CP 4 however is a saddle point in the *GMSK* model and in both the *PZN* and *BFN* subsystems.

[66] The critical points of the *PZN* and *BFN* subsystems describe all of the critical points of the *GMSK* model. The locations of the critical points of the *BFN* subsystem are identical to those of critical points CP 2, CP 3, and CP 4 of the *GMSK* model. Similarly, the locations of two of the critical points of the *PZN* model are identical to those of critical points CP 4 and CP 5 of the *GMSK* model, and the stable spiral point that determines the dynamics of the *PZN* model is very close to CP 1 of the *GMSK* model.

[67] The stability characteristics of the critical points are summarized in Table 2. These reveal that the attractor of the *GMSK* ecosystem model may be considered as the interaction between the attractors of the two subsystems. The *PZN* subsystem is characterized by a stable spiral point that attracts all initial conditions to it. In contrast, the *BFN* subsystem does not have any stable points, but appears to have a limit cycle to which all initial conditions are attracted. The two subsystems are coupled by sharing the saddle critical point CP 4, and by the perturbing influence of *B* on the stability properties of CP 1. This shifts CP 1 of the *PZN* subsystem to the nearby CP 1 point of the *GMSK* model, which is then a saddle point. The *BFN* subsystem also adds two unstable nodes to the *PZN* subsystem. The addition of the *BFN* subsystem to the *PZN* subsystem therefore causes the loss of the stability properties of the *PZN* subsystem, and is an over-all destabilizing influence.

3.2. Sulphur Submodel

[68] The equations of state describing the changes in time of the concentrations of the sulphur compartments (*DMSP* and *DMS*) in the *GMSK* model (equations (7) and (8)) are coupled to the nitrogen components by unidirectional linkages. These equations may therefore be considered separately from the nitrogen compartments, as their dynamics do not affect those of the nitrogen compartments, but passively follow the nitrogen dynamics.

[69] The steady states of the sulphur components of the *GMSK* model (equations (7) and (8)) are given by equations (69) and (70).

$$DMSP^* = \frac{k_5 P + k_{21} Z}{k_{27} + k_{31}} \quad (69)$$

$$DMS^* = \frac{k_6 P + k_{27} DMSP^*}{k_{28} + k_{29} + k_{30}} \quad (70)$$

Substituting equation (69) into equation (70) gives

$$DMS^* = \frac{P(k_5 k_{27} + k_6 k_{27} + k_6 k_{31}) + k_{21} k_{27} Z}{(k_{27} + k_{31})(k_{28} + k_{29} + k_{30})}, \quad (71)$$

which involves only state values of the nitrogen submodel and parameter values.

[70] The stability of the sulphur submodel is given by the eigenvalues of the coefficient matrix of the *DMSP* and *DMS* equations of state,

$$\begin{aligned} \lambda_{S-1} &= -(k_{27} + k_{31}) \\ \lambda_{S-2} &= -(k_{28} + k_{29} + k_{30}). \end{aligned} \quad (72)$$

These eigenvalues are always negative, indicating that the critical point given by equations (69)–(71) is always an asymptotically stable node. For the parameter set used in this analysis, $\lambda_{S-1} = -3.82$ and $\lambda_{S-2} = -6.37$, indicating that the steady state is a strong attractor and the system will return to its equilibrium state rapidly after perturbation (i.e., it is highly resilient). The sulphur submodel dynamics are therefore slaved to, and will closely follow, the dynamics of the biological model.

[71] Both equation (71) derived from the model and equation (21) derived empirically by *Simo and Dachs* [2002] denote a linear relationship between *DMS* and chlorophyll concentrations. As linear correlations between *DMS* and chlorophyll have not been detected in analysis of global data sets [*Kettle et al.*, 1999], the influences of the mixed layer depth in equation (21) and zooplankton in equation (71) are important. The relationship between the two equations is not clear, as all the parameters in equation (71) are rate parameters associated with *DMS* and *DMSP* that are independent of depth. Substituting scaled parameter values into equation (71) reveals that the phytoplankton in the model contributes approximately 2.75 times as much *DMS* as do the same quantity of zooplankton at steady state,

$$DMS^* = 0.0077 P + 0.0028 Z. \quad (73)$$

This equation does not however indicate that field studies should reveal that *DMS* concentration is linearly related to chlorophyll concentration. It can be readily seen in Figure 5a that the relative concentrations of *P* and *Z* are continually changing. The model predicts that during the initial stages of a phytoplankton bloom (the trajectory between CP4 and CP5 in Figure 5a) the phytoplankton population dominates the zooplankton population, and the concentration of *DMS* will be closely related to that of phytoplankton. However, most phytoplankton blooms only last in the order of days, and the region of Figure 5a around CP1, where the system spends most of its time, will determine the relationship between the *DMS* and phytoplankton concentrations. In this region, *P* fluctuates between approximately 0.05 and 0.3, with an equilibrium value of 0.17, while *Z* fluctuates between 0.2 and 0.55, with an equilibrium value of 0.34. While the system is in this region, the determination of *DMS* ranges from 20% due to

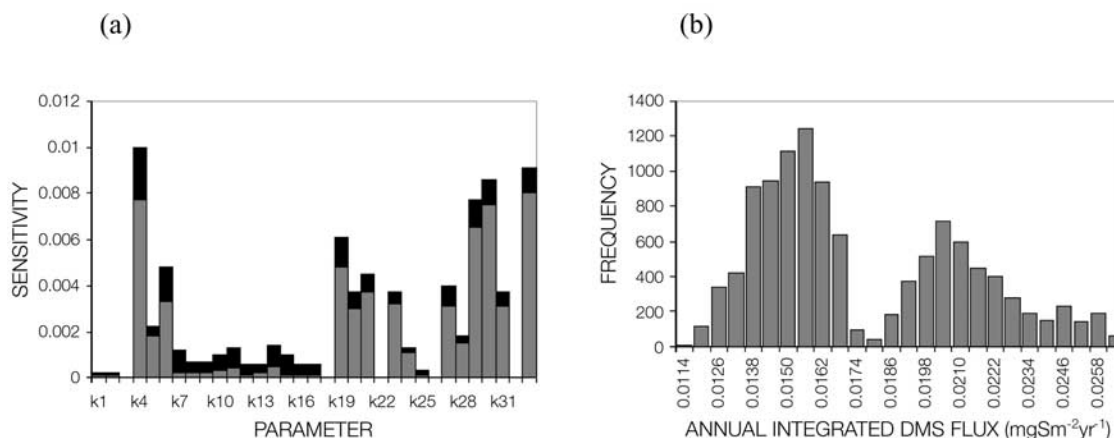


Figure 6. (a) Sensitivity (sum of first- and second-order effects) of integrated annual DMS flux from GMSK model to changes in parameter values. Shaded area is value of first-order effects (μ); black area is value of second-order effects (σ). (b) Uncertainty in integrated annual DMS flux (dimensionless) from GMSK model to changes in parameter values ($n = 11,220$).

P and 80% due to Z , to 80% due to P and 20% due to Z , with an average determination of 57% due to P and 43% due to Z . This suggests that unless DMS and phytoplankton are sampled only during the early stages of a phytoplankton bloom, DMS and phytoplankton concentrations will not generally be linearly dependent. It should also be noted that the apportionments above may be dramatically altered by variations in parameter values that would be associated with different ecosystems, and further modified by the different interactions between endogenous and exogenous dynamics that occur at different latitudes.

[72] It should be recalled here that the phytoplankton sulphur (DMSP) to nitrogen ratio (k_{33}), while not appearing explicitly in equation (71), affects the steady state DMS^* concentration due to its inclusion in the scaling term for the sulphur state variables ($S_0 = k_{33}N_0$). Equation (71) therefore also reveals that DMS^* is linearly dependant on k_{33} .

3.3. Sensitivity Analyses

[73] The results of the sensitivity analysis of the depth-averaged model are presented in Figure 6a, where the “sensitivity” of a parameter is just the sum of the first- and second-order effects. Figure 6a reveals both the influence of the parameters independently (shaded part of column), and the overall influence of each parameter alone and in interaction with all other parameters (black part of column). Four parameters, k_{33} , k_4 , k_{30} , and k_{29} , stand out as having the most influence both individually and in conjunction with other parameters.

[74] The biotic sulphur as DMSP to nitrogen ratio (k_{33}) is the most influential factor on the annual integrated flux of DMS to the atmosphere. The next three parameters include the Z grazing rate on P (k_4), the piston velocity controlling the DMS flux across the air-water interface (k_{30}), and the rate of photo-oxidation of DMS (k_{29}). The 13 most influential parameters of the GMSK model are the 13 parameters of the P , Z , and DMS steady state equations (equations (47), (48), and (71)).

[75] The zooplankton grazing rate on phytoplankton (k_4) has the most influence in two-factor interactions. Examination of the two-factor interactions reveals that k_4 is involved in both of the most significant two-factor interactions, in combination with the first and third most influential single parameters k_{30} and k_{33} . Each of these latter parameters are also involved in significant two-factor interactions with influential single parameters such as k_{29} , but interestingly their own two-factor interaction (k_{30} with k_{33}) ranks 86th in influence of the 528 factor pairs.

[76] A frequency distribution of the integrated annual DMS flux from the 11,220 model evaluations is shown in Figure 6b. The bimodal distribution evident in Figure 6b appears reflect the influence of the two subsystems in the GMSK model noted above, and may be due to the relative amounts of time the system spends on different parts of the attractor. The magnitude of the DMS flux to the atmosphere is primarily determined by the proportion of time that the system spends on the PZN part of the attractor, as little is produced during the proportion spent on the BFN part. The left mode of the distribution in Figure 6b would then derive from parameterizations for which the model spends relatively more time on the part of its attractor associated with the BFN subsystem. The right mode would then represent model parameterizations that traverse the BFN region of the attractor rapidly, and spend proportionally more time approaching the PZN equilibrium. The very clear difference between the modal distributions in Figure 6b may be indicative of potential catastrophic behavior in the GMSK model. A small change in one parameter or in a combination of parameters may result in substantial changes in the output by causing the system to shift from the state represented by one modal distribution to the state represented by the other.

3.4. One-Dimensional Model

[77] The static forcing one-dimensional model simulation reveals that the essential dynamics of the nitrogen submodel noted in Figure 5 are observed in the one-dimensional

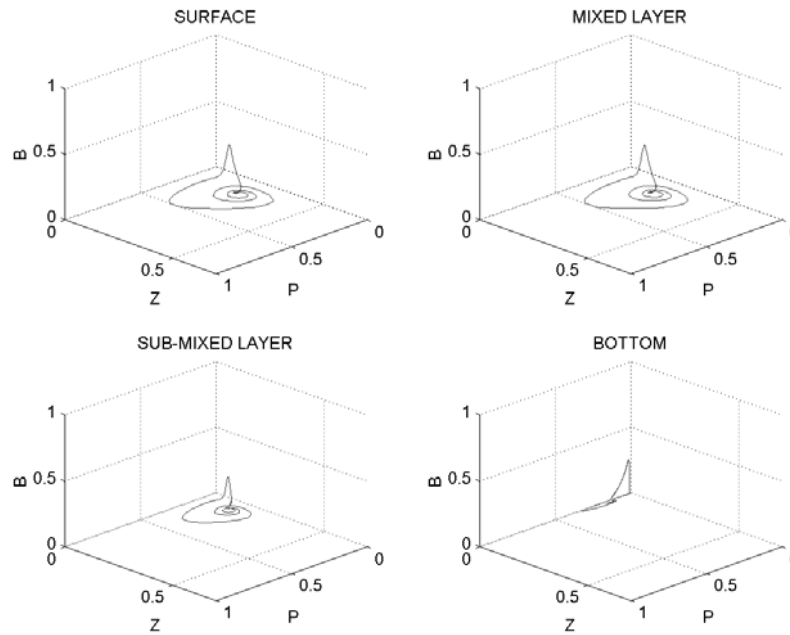


Figure 7. Attractor of the static forcing, one-dimensional GMSK model in PZB space at sea surface, middle of the mixed layer, middle of the sub-mixed layer, and at the bottom boundary. See color version of this figure in the HTML.

model in the absence of temporally varying forcings (Figure 7). The size of the attractor in Figure 5 is, however, slightly modified at each depth in Figure 7; in particular, the amplitudes of the blooms evidenced by the phytoplankton, zooplankton, and bacteria are all substantially reduced from the depth-averaged GMSK model. This is largely due to the effects of the reduced average irradiance received by phytoplankton in the one-dimensional model. In this case, phytoplankton are mixed down to 50 m where light levels are about 10% of the incident surface irradiance, and their growth is limited by equation (10). This reduction in primary production subsequently impacts on the other biota in the model, resulting in reduced bloom amplitudes compared to the depth-averaged model. This is particularly evident in the zooplankton concentration at the bottom boundary (Figure 7), which does not bloom at all, despite an apparent small phytoplankton bloom.

[78] The one-dimensional model simulations generated realistic depth profiles of the state variables (Figure 8) when forced by high-latitude seasonal forcings of photosynthetically available radiation, sea surface temperature, mixed layer depth, and sea surface wind (60°S–70°S panels in Figures 1–4). These forcings effectively overwhelm the endogenous dynamics of the one-dimensional model. The model dynamics will therefore vary zonally, with the endogenous model dynamics observed near the equator where the amplitudes of seasonal forcings are low. At high latitudes, the large-amplitude seasonal forcings overwhelm the endogenous dynamics and essentially control the evolution of the state variables.

[79] The comparisons of sea surface DMS predicted by the model and that predicted by the empirical relationship

of *Simo and Dachs* [2002] are presented in Table 3 and Figure 9. For these comparisons, k_{33} has been calibrated so that the slope of the regression equating the model DMS concentrations and the *Simo and Dachs* concentrations in each zone are unity. The values of k_{33} required to achieve this are listed in Table 3. This parameter was identified by the sensitivity analysis above as the single most influential parameter in the model, and DMS concentration scales linearly with it. Values of k_{33} calculated for individual species reported by *Gabric et al.* [1993] ranged from 0.01 for *Thalassiosira sp.* to 0.71 for *Melosira nummuloides*, about half the maximum value required to meet the criteria of our analysis.

[80] These results reveal that the DMS predicted by the model correlates very closely with the predictions of *Simo and Dachs*' [2002] equations. Some of the discrepancies between *Simo and Dachs* and the model DMS predictions may be attributable to differences in ecosystem parameters. These parameters vary spatially, reflecting differences in ecosystem structure and constituent biota. Recent work by *Gabric et al.* [2003] inferred some of these parameters by inverting a simple (PZN) depth-averaged ecosystem model to match satellite chlorophyll data. This work revealed zonal trends in ecosystem parameters. Unfortunately, there are insufficient data available to calibrate the one-dimensional model, even on a zonal basis. However, simple depth-averaged model parameters are relatively easy to calibrate to a specific location, and when this is done, DMS predictions that closely match those of *Simo and Dachs*' equations are obtained [*Gabric et al.*, 2003]. This can also remove much of the hysteresis evident in Figure 9 in mid- to high-latitude zones.

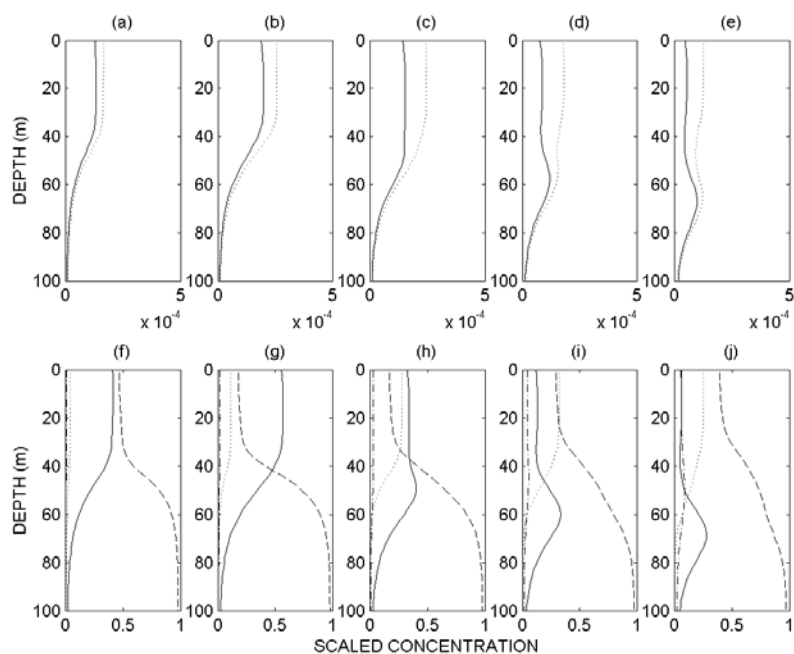


Figure 8. (a–e) Depth profiles of DMSP and DMS (dotted and solid lines, respectively) and (f–j) P , B , Z , and N (solid, dot-dashed, dotted, and dashed lines, respectively) for days 60 (Figures 8a and 8f), 70 (Figures 8b and 8g), 80 (Figures 8c and 8h), 90 (Figures 8d and 8i), and 100 (Figures 8e and 8j) of the seasonally forced one-dimensional model. Concentrations have been scaled as described for the GMSK model.

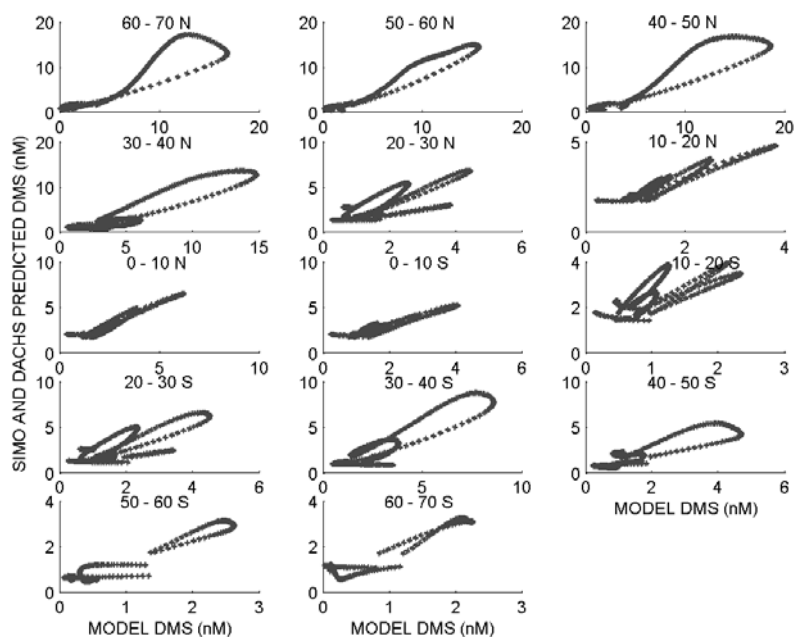


Figure 9. Scatterplots of DMS sea surface concentrations predicted by the model and those predicted from *Simo and Dachs* [2002] equations. See color version of this figure in the HTML.

Table 3. Comparisons Between DMS Sea Surface Concentration Predicted by the Model and That Predicted by *Simo and Dachs* [2002] for 10° Zones Between 70°N and 70°S^a

Zone	r^2	k_{33}	Equation (20)	Equation (21)
70°N–60°N	0.88	1.5724	244	121
60°N–50°N	0.96	1.5142	233	132
50°N–40°N	0.90	1.884	201	164
40°N–30°N	0.85	1.6105	156	209
30°N–20°N	0.52	0.5194	95	270
20°N–10°N	0.90	0.4209	52	313
10°N–0°	0.95	0.6745	15	350
0°–10°S	0.88	0.4478	53	312
10°S–20°S	0.58	0.2723	110	255
20°S–30°S	0.50	0.4909	124	241
30°S–40°S	0.81	0.883	177	188
40°S–50°S	0.83	0.4401	245	120
50°S–60°S	0.96	0.2418	290	75
60°S–70°S	0.93	0.2174	280	85

^aThe values for equations (20) and (21) refer to the number of times each equation was applied in each zone.

[81] Table 3 reveals that equation (20) is applied more frequently than equation (21) in high-latitude zones, but equation (21) is applied more frequently than equation (20) in low-latitude zones, with a gradual change between zones through the midlatitudes. This is largely due to the very deep winter mixed layer depths observed at high latitudes (Figure 2) causing winter chlorophyll to MLD ratios to be less than 0.02. Equation (21) is only applied during summer at high latitudes when the mixed layer depth shallows and substantial phytoplankton blooms eventuate.

[82] The model predictions are highly positively correlated with the *Simo and Dachs* [2002] prediction in all latitude zones, but are slightly lower around 20°–30° either side of the equator. We are unable to explain this phenomenon at present, but note that it is not due to differences in the number of times each equation is applied, as there is a monotonic trend from the equator to the poles in each hemisphere in this respect. Similarly, it is unlikely to be a result of variations in the forcings as these also vary smoothly with latitude zone.

[83] As we have used the mixed layer depth data used to force the one-dimensional GMSK model and phytoplankton predicted by the model as inputs to calculate DMS from the *Simo and Dachs* [2002] algorithm, we should consider if this has influenced the correlations observed in our analysis. As noted above, the eigenvalues of the sulphur submodel are large and negative, and this model may be considered slaved to the nitrogen-based components of the GMSK model. The DMS predicted by the model is therefore well described by equation (71). Although the *Simo and Dachs* relationships are not dimensionally consistent, we can qualitatively compare equation (71) with equations (20) and (21). Although phytoplankton is linearly related to DMS in both equations (21) and (71), the equations represent very different dependencies of DMS on phytoplankton. In equation (21) the quantity of DMS generated by a given quantity of phytoplankton varies as inverse of the mixed layer depth, whereas in equation (71) a given quantity of phytoplankton always produces the same quantity of

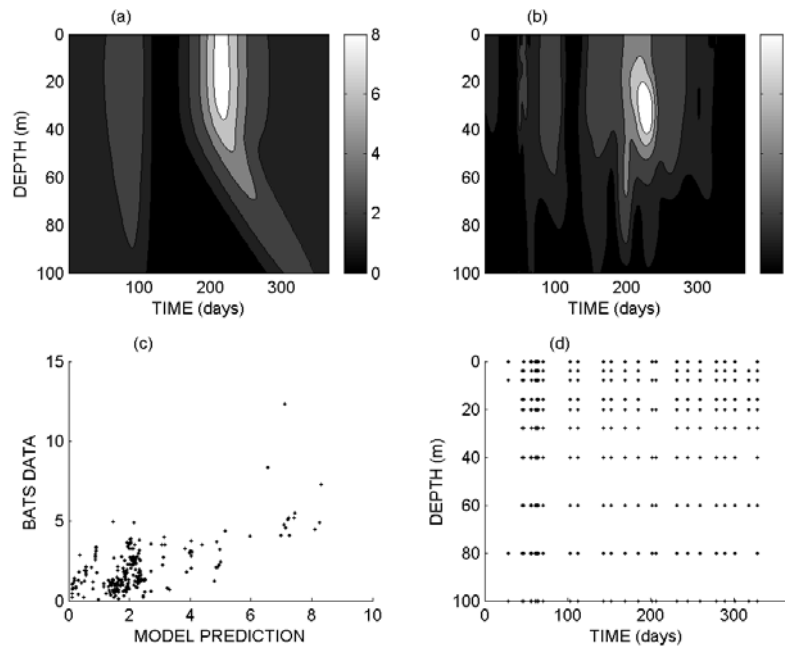


Figure 10. Comparison of time series of water column concentrations of DMS produced by the model with those measured at BATS. The depth-time distribution of DMS concentration (a) produced by the model and (b) interpolated from the BATS data. (c) Scatterplot of BATS measurements and model predictions at same time and depth points, and (d) depth-time location of BATS measurements. Contour lines are drawn at 1, 2, 4, 6, and 8 nM in Figures 10a and 10b.

Table 4. Calibrated Parameter Values Used to Fit BATS Data

Parameter	Process	Units	Old Value	New Value
k_4	Z grazing rate (per individual) on P	$\text{m}^3 \text{mgN}^{-1} \text{d}^{-1}$	0.010	0.0137
k_{19}	Z specific N excretion rate	d^{-1}	0.050	0.0177
k_{20}	proportion of N uptake excreted by Z		0.400	0.8096
k_{23}	maximum rate of N uptake by P	d^{-1}	0.270	0.2392
k_{29}	maximum DMS photo-oxidation rate	d^{-1}	1.300	0.9267
k_{33}	phytoplankton S(DMSP):N ratio		0.300	0.8000
k_v	phytoplankton sinking velocity	n d^{-1}	0.500	0.3559
I_s	phytoplankton saturating irradiance	W m^{-2}	60	71

DMS, which may be added to by contributions from zooplankton. As noted above, zooplankton may produce 20–80% of the DMS in the model simulations, but on average produces 43%. It is obvious from Figure 5 that phytoplankton and zooplankton exhibit substantial temporal variation and the DMS predicted by the model will not be simply related to phytoplankton.

[84] Equation (20), on the other hand, predicts DMS as a function of the logarithm of the mixed layer depth, and it is difficult to see how this relates to equation (71). Table 3 indicates that the model describes 50–96% of the variation in the *Simo and Dachs* [2002] predictions. The model's efficacy is apparently independent of which of *Simo and Dachs'* equations is utilized most frequently in the calculation (i.e., compare 10°N – 0° with 50°S – 60°S). As *Simo and Dachs* [2002] observed that equations (20) and (21) reproduced observed DMS data very accurately in their study, we consider the close correlations between our model DMS and that produced by the *Simo and Dachs* algorithm to reflect the veracity of the interaction of the model ecosystem and the physical forcings with regard to the production of DMS. This consideration lies at the heart of the model's ability to predict the possible effects of biogenic DMS on climate.

[85] The comparison of the one-dimensional model output with the BATS data is presented in Figure 10. The model output was generated using the same zonal forcings for 30°N – 40°N used for the comparison with the *Simo and Dachs* [2002] relationship above, but with eight of the 35 parameters calibrated to provide the “best fit” to the BATS data. The best fit criteria in this case was specified to be a least squared error, which resulted in the slope of the regression line of the 247 BATS data points and the model prediction at the same points approximately equal to 1. The eight parameters were selected for calibration on the basis of the results of the sensitivity analysis of the zero-dimensional model and the inclusion of two parameters that we predicted would influence the timing and depth of the DMS maximum. These parameters and their calibrated values are presented in Table 4.

[86] The results of the comparison are presented in Figure 10 and Table 5. Figure 10a shows the DMS concentrations predicted by the model over depth and time for 1 year after a 1-year integration to eliminate the effects of the initial conditions. This may be compared to Figure 10b, in which the 247 BATS data points have been interpolated to match the temporal and spatial density of the 9490 model results. As the BATS data

points represent only 2.6% of the interpolated points, these have been smoothed to remove some of the fine structure that is an artifact of the interpolation. Despite this, comparison of Figure 10b with the location of the BATS data measurements in time and space (Figure 10d) reveals that artifacts of the interpolation may still be present in Figure 10b. Although a useful method of displaying the BATS data for comparison with the model, only the broad scale structure evident in Figure 10b is therefore useful for comparison. Figure 10c demonstrates the close relation between the 247 BATS measurements and the model prediction at those points. A linear regression of the data shown in Figure 10c has a slope of 1.06 and indicates that the model explains up to 44% of the variation in the measured data.

[87] The broad scale structures of Figures 10a and 10b are quite similar, with both the model and data evidencing a broad, low concentration DMS peak at about day 80–100 and a clearly defined, high concentration DMS peak at about day 230. The large bloom occurs at a depth of 30 m on day 232 in the BATS data, and at a depth of 24 m on day 216 in the model predictions. The maximum in the BATS data is largely attributable to one data point with a very high concentration (approximately 7 standard deviations above the mean and 50% higher than the next highest concentration) on day 232. Owing to the few data defining the maximum, and the paucity of data in the preceding 46 days, we elected not to calibrate the model to reproduce the timing exactly (although this was possible), but to improve the overall variation explained by the model. Figure 10 and Table 5 reveal that the model does a good job of reproducing the major characteristics of the BATS data. As the model only explains 44% of the variation in the data, it does not do a good job of reproducing the fine detail, but this is to be expected as the model uses a homogeneous mixed layer specified by

Table 5. Comparison of Model Predictions With BATS Data

Feature	Model	BATS
Mean DMS concentration, nM	2.0	1.9
Standard deviation of DMS concentration, nM	1.7	1.5
Maximum concentration, nM	8.9	12.3
Day of maximum concentration (day of year)	216	232
Depth of maximum concentration, m	24	30

equation (18) and does not resolve many of the factors that lead to fine-scale variations in DMS concentration.

4. Discussion

[88] Our analysis indicates that the GMSK model may be considered as three coupled submodels: a *PZN* submodel, a *BFN* submodel, and a DMS submodel. The *PZN* and *BFN* submodels are linked, with the dynamics of the GMSK model closely related to the critical points of the two submodels. The state of the GMSK model alternately traverses the *PZN* part of the attractor where DMS is predominantly produced and then the *BFN* part of the attractor where DMS is predominantly consumed. In switching between these two parts of the attractor, a scenario where bacterial blooms precipitate the rapid collapse of phytoplankton and zooplankton populations is simulated. There appears to be little evidence of bacteria initiating the collapse of phytoplankton and zooplankton populations in real marine ecosystems [see, e.g., *Ducklow*, 1994], and this behavior has been a source of criticism of the GMSK model [*Watts and Bigg*, 2001]. However, the influence of bacteria is substantially reduced when the GMSK model is extended to include a vertical dimension and is forced in realistic seasonal scenarios; then bacterial-induced population collapses are no longer evident.

[89] Our analysis also indicates that the GMSK model's DMS production may be well described by a linear combination of phytoplankton and zooplankton biomasses, as the DMS submodel is effectively slaved to the *PZN* submodel by its large negative eigenvalues. These eigenvalues are determined by the rates of loss of DMSP and DMS to sinks such as photo-oxidation, bacterial consumption, and emission to the atmosphere. The complicated dynamics of the ecosystem component of the GMSK model suggest that the linear relationship between DMS and phytoplankton and zooplankton does not imply that DMS and phytoplankton alone will exhibit a linear relationship. Empirical testing of this relationship in the field would provide a rigorous evaluation of the GMSK representation of DMS production processes and may provide a useful insight into the factors determining DMS concentration in the ocean.

[90] The sensitivity of the GMSK model to both individual parameters and combinations of parameters confirms that the *B* and *F* compartments, and therefore the dynamics of the *BFN* system, are not important determinants of the magnitude of the modeled DMS flux to the atmosphere. The most important parameters influencing DMS production and emission to the atmosphere are the phytoplankton sulphur as DMSP to nitrogen ratio (k_{33}) and zooplankton grazing rate (k_4), which also reflects phytoplankton palatability. The attributes of the species dominating a phytoplankton community will therefore be a significant determinant of the ecosystem's production of DMS. Important physical factors are the sea-air DMS piston velocity (k_{30}) and the DMS photo-oxidation rate (k_{29}), a still poorly understood parameter [*Gabric et al.*, 2001a]. Our analysis suggests that these

parameters must be better understood before we can reliably predict the contribution that biogenic DMS might make to climate regulation.

[91] The strong dependence of the modeled DMS on the phytoplankton community structure, while explicitly represented in the model by variations in the values of biotic parameters, is not explicit in the algorithm of *Simo and Dachs* [2002]. However, changes in mixed layer depth can precipitate profound changes in the composition of the mixed layer phytoplankton community [*Margalef*, 1978] and food web structure [*Kjorboe*, 1993]. These changes may therefore be implicit in equations (20) and (21).

[92] The bimodal distribution of model outputs obtained from the sensitivity analysis suggests that the GMSK model has the potential for catastrophic behavior. The distinct separation between the two distributions suggests that the variation of one parameter, or a combination of several parameters, may shift the system from a high DMS production state to a lower one. Examination of the model dynamics suggests that this shift involves the system residing on different parts of the same attractor for different proportions of time, rather than switching between attractors. Determination of the parameter sets that control this behavior will be a topic of future work.

[93] Incorporation of the vertical spatial dimension in the GMSK model to resolve the influence of variations in the mean light regime experienced by the phytoplankton due to changes in the mixed layer depth and diffusivity does not affect the fundamental nature of the model's dynamics. Similarly, subjecting the one-dimensional model to realistic seasonally varying forcings of sea surface temperature and photosynthetically available radiation has little effect on the endogenous dynamics in equatorial regions due to the small amplitude of the forcings. However, in high latitudes, where seasonal forcings are typically of large amplitude, the endogenous dynamics are overwhelmed and the model exhibits dynamics that are substantially controlled by the external forcings.

[94] Our investigations with zonal physical forcings provide realistic simulations that include model dynamics ranging from predominantly endogenous control to predominantly exogenous control. Comparisons of model simulations of sea surface DMS concentrations with those predicted by the empirical relationship of *Simo and Dachs* [2002] show remarkably close agreement. The one-dimensional GMSK model therefore appears to capture the important processes controlling ecosystem dynamics and consequent DMS production over the region of global ocean between 70°N and 70°S, the range for which reliable mixed layer depth data are available.

[95] Comparison of the calibrated one-dimensional model results with vertical profiles of DMS measured at BATS also reveals that the model does a good job resolving spatial and temporal variations in DMS concentration. The model predicted the mean and standard deviation of the annual concentration of DMS accurately, as well as explaining up to 44% of the variation in the observed data. It also accurately predicted the timing and depth of major and

minor peaks in DMS concentration, but underestimated the magnitude of the peaks. This may be in part due to the model using a homogeneous mixed layer that prevented it from resolving the finer detail of the spatial and temporal variation of the BATS data.

[96] The multifaceted approach employed in our evaluation of the GMSK model has provided insights into the important mechanisms in the model that would not have become evident if we had just evaluated the model's ability to reproduce observed data. These insights may provide useful information for the design of future field studies and may also provide an opportunity to rigorously test the process representation of the GMSK model.

[97] **Acknowledgments.** The authors would like to thank the SeaWiFS Project (code 970.2) and the Distributed Active Archive Center (code 902) at the Goddard Space Flight Center, Greenbelt, Maryland, for the production and distribution of the SeaWiFS data, respectively. These activities are sponsored by NASA's Mission to Planet Earth Program (<http://seawifs.gsfc.nasa.gov>). The Advanced Very High Resolution Radiometer data were obtained from the NASA Physical Oceanography Distributed Active Archive Center at the Jet Propulsion Laboratory/California Institute of Technology (<http://podaac.jpl.nasa.gov>). The mixed layer depth data were provided by the Carbon Dioxide Information Analysis Center, Oak Ridge National Laboratory, Tennessee (<http://cdiac.ornl.gov/ftp/ndp076>).

References

- Boyce, W. E., and R. C. DiPrima (1997), *Elementary Differential Equations and Boundary Value Problems*, 749 pp., John Wiley, Hoboken, N. J.
- Campolongo, F., and R. Braddock (1999), The use of graph theory in the sensitivity analysis of the model output: A second order screening method, *Reliab. Eng. Syst. Safety*, **64**, 1–12.
- Campolongo, F., and A. Saltelli (1997), Sensitivity analysis of an environmental model: An application of different analysis methods, *Reliab. Eng. Syst. Safety*, **57**, 49–69.
- Charlson, R. J., J. E. Lovelock, M. O. Andreae, and S. G. Warren (1987), Oceanic phytoplankton, atmospheric sulphur, cloud albedo and climate, *Nature*, **326**, 655–661.
- Cropp, R. A., and R. D. Braddock (2002), The New Morris Method: An efficient second-order screening method, *Reliab. Eng. Syst. Safety*, **78**, 77–83.
- Dacey, J. W. H., F. A. Howes, A. F. Michaels, and S. G. Wakeham (1998), Temporal variability of dimethylsulfide and dimethylsulfoniopropionate in the Sargasso Sea, *Deep Sea Res., Part I*, **45**, 2085–2104.
- Denman, K. L., and M. A. Pena (1999), A coupled 1-D biological/physical model of the northeast subarctic Pacific Ocean with iron limitation, *Deep Sea Res., Part II*, **46**, 2877–2908.
- Doney, S. C., D. M. Glover, and R. G. Najjar (1996), A new coupled, one-dimensional biological-physical model for the upper ocean: Applications to the JGOFS Bermuda Atlantic Time-series Study (BATS) site, *Deep Sea Res., Part II*, **43**, 591–624.
- Druon, J., and J. Le Fevre (1999), Sensitivity of a pelagic ecosystem model to variations of process parameters within a realistic range, *J. Mar. Syst.*, **19**, 1–26.
- Ducklow, H. W. (1994), Modeling the microbial loop, *Microbial Ecol.*, **28**, 303–319.
- Edwards, C. A., T. A. Powell, and H. P. Batchelder (2000), The stability of an NPZ model subject to realistic levels of vertical mixing, *J. Mar. Res.*, **58**, 37–60.
- Eigenheer, A., W. Kuhn, and G. Radach (1996), On the sensitivity of ecosystem box model simulations on mixed-layer depth estimates, *Deep Sea Res., Part I*, **43**, 1011–1027.
- Eppley, R. W. (1972), Temperature and phytoplankton growth in the sea, *Fish. Bull.*, **70**(4), 1063–1085.
- Evans, G. T., and V. Garçon (1997), One-dimensional models of water column biogeochemistry, *JGOFS Rep.* **23**, 84 pp., Sci. Comm. on Oceanic Res. Int. Counc. of Sci. Unions, Toulouse, France.
- Fennel, K., M. Losch, J. Schroter, and M. Wenzel (2001), Testing a marine ecosystem model: Sensitivity analysis and parameter optimisation, *J. Mar. Syst.*, **28**, 45–63.
- Gabric, A. J., and J. Parslow (1989), Effect of physical factors on the vertical distribution of phytoplankton in eutrophic coastal waters, *Aust. J. Mar. Freshwater Res.*, **40**, 559–569.
- Gabric, A. J., N. Murray, L. Stone, and M. Kohl (1993), Modeling the production of dimethylsulfide during a phytoplankton bloom, *J. Geophys. Res.*, **98**(C12), 22,805–22,816.
- Gabric, A. J., P. A. Matrai, and M. Vernet (1999), Modelling the production and cycling of dimethylsulphide during the vernal bloom in the Barents Sea., *Tellus, Ser. B*, **51**, 919–937.
- Gabric, A., W. Gregg, R. Najjar, D. Erickson, and P. A. Matrai (2001a), Modeling the biogeochemical cycle of dimethylsulfide in the upper ocean: A review, *Chemos. Global Change Sci.*, **3**, 377–392.
- Gabric, A. J., P. H. Whetton, and R. A. Cropp (2001b), Dimethylsulphide production in the subantarctic Southern Ocean under enhanced greenhouse conditions, *Tellus, Ser. B*, **53**, 273–287.
- Gabric, A. J., R. A. Cropp, A. C. Hirst, and H. J. Marchant (2003), The response of dimethylsulphide production to simulated warming in the eastern Antarctic Southern Ocean, *Tellus, Ser. B*, **55**, 966–981.
- Goldman, J. C., and E. L. Carter (1974), A kinetic approach to the effect of temperature on algal growth., *Limnol. Oceanogr.*, **19**, 756–766.
- Goyet, C., R. J. Healy, and J. P. Ryan (2000), Global distribution of total inorganic carbon and total alkalinity below the deepest winter mixed layer depths, report, Carbon Dioxide Inf. Anal. Cent., Oak Ridge Natl. Lab., Oak Ridge, Tenn.
- Holland, J. H. (1975), *Adaptation in Natural and Artificial Systems*, 211 pp., Univ. of Mich. Press, Ann Arbor.
- Jodwalis, C. M., R. L. Benner, and D. L. Eslinger (2000), Modeling the dimethylsulfide ocean mixing, biological production, and sea-to-air flux for high latitudes, *J. Geophys. Res.*, **105**(D11), 14,387–14,399.
- Kettle, A. J., and M. O. Andreae (2000), Flux of dimethylsulfide from the oceans: A comparison of updated data sets and flux models, *J. Geophys. Res.*, **105**(D22), 26,703–26,808.
- Kettle, A. J., et al. (1999), A global database of sea surface dimethylsulfide (DMS) measurements and a procedure to predict sea surface DMS as a function of latitude, longitude and month, *Global Biogeochem. Cycles*, **13**, 399–444.
- Kiorboe, T. (1993), Turbulence, phytoplankton cell size, and the structure of pelagic food webs, *Adv. Mar. Biol.*, **29**, 1–72.
- Lefevre, M., A. Vezina, M. Levasseur, and J. W. H. Dacey (2002), A model of dimethylsulfide dynamics for the subtropical North Atlantic, *Deep Sea Res., Part I*, **49**, 2221–2239.
- Liss, P. S., and L. Merlivat (1986), Air-sea gas exchange rates: Introduction and synthesis, in *The Role of Air-Sea Exchange in Geochemical Cycling*, edited by P. Baut-Menard, pp. 113–127, D. Reidel, Norwell, Mass.
- Mann, K. H., and J. R. N. Lazier (1996), *Dynamics of Marine Ecosystems*, 394 pp., Blackwell Sci., Cambridge, Mass.
- Margalef, R. (1978), Life-forms of phytoplankton as survival alternatives in an unstable environment, *Oceanol. Acta*, **1**, 493–509.
- Martin, P. J. (1985), Simulation of the mixed layer at OWS November and Papa with several models, *J. Geophys. Res.*, **90**(C1), 903–916.
- Martin, P. J. (1986), Testing and comparison of several mixed-layer models, report, Naval Oceanogr. and Atmos. Res. Lab., Stennis Space Center, Miss.
- Matrai, P. A., and M. Vernet (1997), Dynamics of the vernal bloom in the marginal ice zone of the Barents Sea: Dimethylsulfide and dimethylsulfoniopropionate budgets, *J. Geophys. Res.*, **102**(C10), 22,965–22,979.
- Oreskes, N., K. Schrader-Frechette, and K. Belitz (1994), Verification, validation and confirmation of numerical models in the Earth sciences, *Science*, **263**, 641–646.
- Pond, S., and S. L. Pickard (2000), *Introductory Dynamical Oceanography*, 329 pp., Butterworth-Heinemann, Woburn, Mass.
- Saltzman, E. S., D. B. King, K. Holmen, and C. Leck (1993), Experimental determination of the diffusion coefficient of dimethylsulfide in water, *J. Geophys. Res.*, **98**(C9), 16,481–16,486.
- Schiesser, W. E. (1991), *The Numerical Method of Lines: Integration of Partial Differential Equations*, Academic, San Diego, Calif.
- Schiesser, W. E. (1994), *Computational Mathematics in Engineering and Applied Science*, CRC, Boca Raton, Fla.
- Shaw, G. E. (1983), Bio-controlled homeostasis involving the sulphur cycle, *Clim. Change*, **5**, 297–303.
- Simo, R., and J. Dachs (2002), Global ocean emission of dimethylsulfide predicted from biogeochemical data, *Global Biogeochem. Cycles*, **16**(4), 1018, doi:10.1029/2001GB001829.

- Simo, R., and C. Pedros-Alio (1999), Role of vertical mixing in controlling the oceanic production of dimethyl sulphide, *Nature*, 402, 396–399.
- Smayda, T. J. (1970), The suspension and sinking of phytoplankton in the sea, *Oceanogr. Mar. Biol. Annu. Rev.*, 8, 353–414.
- Spitz, Y. H., J. R. Moisan, and M. R. Abbott (2001), Configuring an ecosystem model using data from the Bermuda Atlantic Time Series (BATS), *Deep Sea Res., Part II*, 48, 1733–1768.
- Walsh, J., D. A. Dieterle, and J. Lenes (2001), A numerical analysis of carbon dynamics of the Southern Ocean phytoplankton community: The roles of light and grazing in effecting both sequestration of atmospheric CO₂ and food availability to larval krill, *Deep Sea Res., Part I*, 48, 1–48.
- Watts, M., and G. Bigg (2001), Modelling the nitrogen cycle and DMS production in Lagrangian experiments in the North Atlantic, *Deep Sea Res., Part II*, 48, 1019–1042.
-
- R. D. Braddock, R. A. Cropp, and A. J. Gabric, Faculty of Environmental Sciences, Griffith University, Kessels Road, Nathan, Queensland 4111, Australia. (r.braddock@griffith.edu.au; r.cropp@griffith.edu.au; a.gabric@griffith.edu.au)
- J. Norbury, Mathematical Institute, University of Oxford, 24-29 St. Giles', Oxford OX1 3LB, UK. (john.norbury@lincoln.ox.ac.uk)